Article

Current Biology

Multi-timescale motor circuit dynamics underlie adaptive and efficient exploratory behavior

Highlights

- *C. elegans* head movements comprise slow rhythmic bends and fast head casts
- RMD neurons drive head casts; SMD and SMB sustain slow rhythmic bending
- Phase-specific head casts correlate with directional changes during locomotion
- Head casts optimize locomotion efficiency by reducing the body's angle of attack

Authors

Pinjie Li, Heng Zhang, Jiaqi Wang, Yifan Su, Louis Tao, Quan Wen

Correspondence

heng.zhang@stu.pku.edu.cn (H.Z.), taolt@mail.cbi.pku.edu.cn (L.T.), qwen@ustc.edu.cn (Q.W.)

In brief

Li, Zhang, et al. analyze head exploratory behavior in *C. elegans*, identifying slow rhythmic bends and fast, phase-specific head casts via variational mode decomposition. Combinatorial motor neuron ablations reveal distinct roles for the RMD, SMD, and SMB neurons. A dual-proprioceptive feedback model shows how head casts optimize locomotion efficiency during exploration.

Li et al., 2026, Current Biology *36*, 1–15
June 22, 2026
https://doi.org/10.1016/j.cub.2026.05.004

CellPress

Please cite this article in press as: Li et al., Multi-timescale motor circuit dynamics underlie adaptive and efficient exploratory behavior, Current Biology (2026), https://doi.org/10.1016/j.cub.2026.05.004

Current Biology

CellPress

Article

Multi-timescale motor circuit dynamics underlie adaptive and efficient exploratory behavior

Pinjie Li,[1,2,5] Heng Zhang,[3,5,6,*] Jiaqi Wang,[1,2,5] Yifan Su,[4,5] Louis Tao,[3,4,*] and Quan Wen[1,2,*]
[1]Division of Life Sciences and Medicine, University of Science and Technology of China, Hefei 230026, China
[2]Hefei National Laboratory for Physical Sciences at the Microscale, Center for Integrative Imaging, University of Science and Technology of China, Hefei 230026, China
[3]Center for Quantitative Biology, Academy for Advanced Interdisciplinary Studies, Peking University, Beijing 100871, China
[4]Center for Bioinformatics, National Laboratory of Protein Engineering and Plant Genetic Engineering, School of Life Sciences, Peking University, Beijing 100871, China
[5]These authors contributed equally
[6]Lead contact
*Correspondence: heng.zhang@stu.pku.edu.cn (H.Z.), taolt@mail.cbi.pku.edu.cn (L.T.), qwen@ustc.edu.cn (Q.W.)
https://doi.org/10.1016/j.cub.2026.05.004

SUMMARY

Motor systems must balance stability and flexibility to enable efficient and adaptive movements, yet the circuit-level mechanisms generating their intrinsic dynamics remain poorly understood. Here, we investigate the head exploratory behavior of *Caenorhabditis elegans*, a minimal system capable of intricate motor patterns. Using variational mode decomposition, we identified two distinct motor dynamics: slow rhythmic bends propagating along the body and fast, phase-specific head casts influencing directional bias. Combinatorial ablations of three classes of cholinergic motor neurons, in conjunction with dynamical systems analysis, revealed their distinct and overlapping roles: RMD contributes to head casts, SMD sustains bending states, and SMB and SMD enable slow rhythmic bending and head-body coupling. Collectively, these neurons form a major rhythm generator that sustains undulatory forward locomotion. We propose a model where dual-proprioceptive feedback operates across multiple timescales, with slow feedback coordinating rhythmic bending and fast feedback shaping head casts to optimize roaming efficiency. Our findings highlight how complex, structured dynamics emerge from highly interactive low-level circuits.

INTRODUCTION

Motor control in animals requires seamless integration of stereotyped patterns with behavioral flexibility.[1–3] Traditional theories focus on hierarchical control, positing that higher brain regions dictate fixed sequences executed by lower circuits.[4–8] Recent research proposes a more integrated view wherein descending commands work in concert with the intrinsic properties of local circuits[9–12] and rich sensory feedback[13,14] to generate actions. This framework not only explains the stability of rhythmic gaits[15–18] but also accounts for the variability and adaptability inherent in natural, exploratory behaviors: for example, when a monkey performs a reaching task,[9] elephants manipulate their trunks to investigate their environment,[19] and humans use quick eye movements to scan their surroundings.[20] This leads to a new set of questions: how can lower-level motor circuits generate the higher-dimensional intrinsic dynamics that facilitate efficient navigation and exploration?

The 1-mm-long nematode *Caenorhabditis elegans* is a compelling model for exploring these questions. In its microscopic world, *C. elegans* uses biased random walks[21] and weathervane strategies[22–24] to locate food by balancing exploration and exploitation.[25–27] "Weathervaning," or klinotaxis, involves gradual, shallow turns during forward locomotion, with head movements being critical for steering.[28–30] Most sensory neurons in *C. elegans* expose their cilia ends at the tip of the head, acting as tiny antennae. This morphological arrangement suggests that each head swing converts spatial cues into temporal codes, which could guide decisions on food, mates, and threats.[31]

Despite the presumed importance of head movements, their nature has remained poorly characterized.[31] Early studies described these head swings as "foraging" behavior[32,33] and noted their suppression during escape responses.[34,35] However, these studies lacked quantitative analysis to determine whether foraging movements are distinct from the animal's regular head oscillations. An important step forward came from Kaplan and colleagues,[36] who revealed that head movements contain nested motor dynamics: rapid "casts" embedded within slower bends, suggesting hierarchical control.[36] This study established that head motor activity is not simply rhythmic but organized across multiple timescales.

However, the functions of *head casts* and the circuit-level mechanisms generating fast and slow dynamics remain largely unknown. The dorsal-ventral head movement in *C. elegans* is mainly driven by three classes of cholinergic motor neurons: RMD, SMD, and SMB. RMD includes six neurons, while SMD and SMB have four each (Figure 1B). Ventral head muscles are innervated by RMDV, SMDV, and SMBV, whereas dorsal muscles are innervated by RMDD, SMDD, and SMBD. RMDL and

Please cite this article in press as: Li et al., Multi-timescale motor circuit dynamics underlie adaptive and efficient exploratory behavior, Current Biology (2026), https://doi.org/10.1016/j.cub.2026.05.004

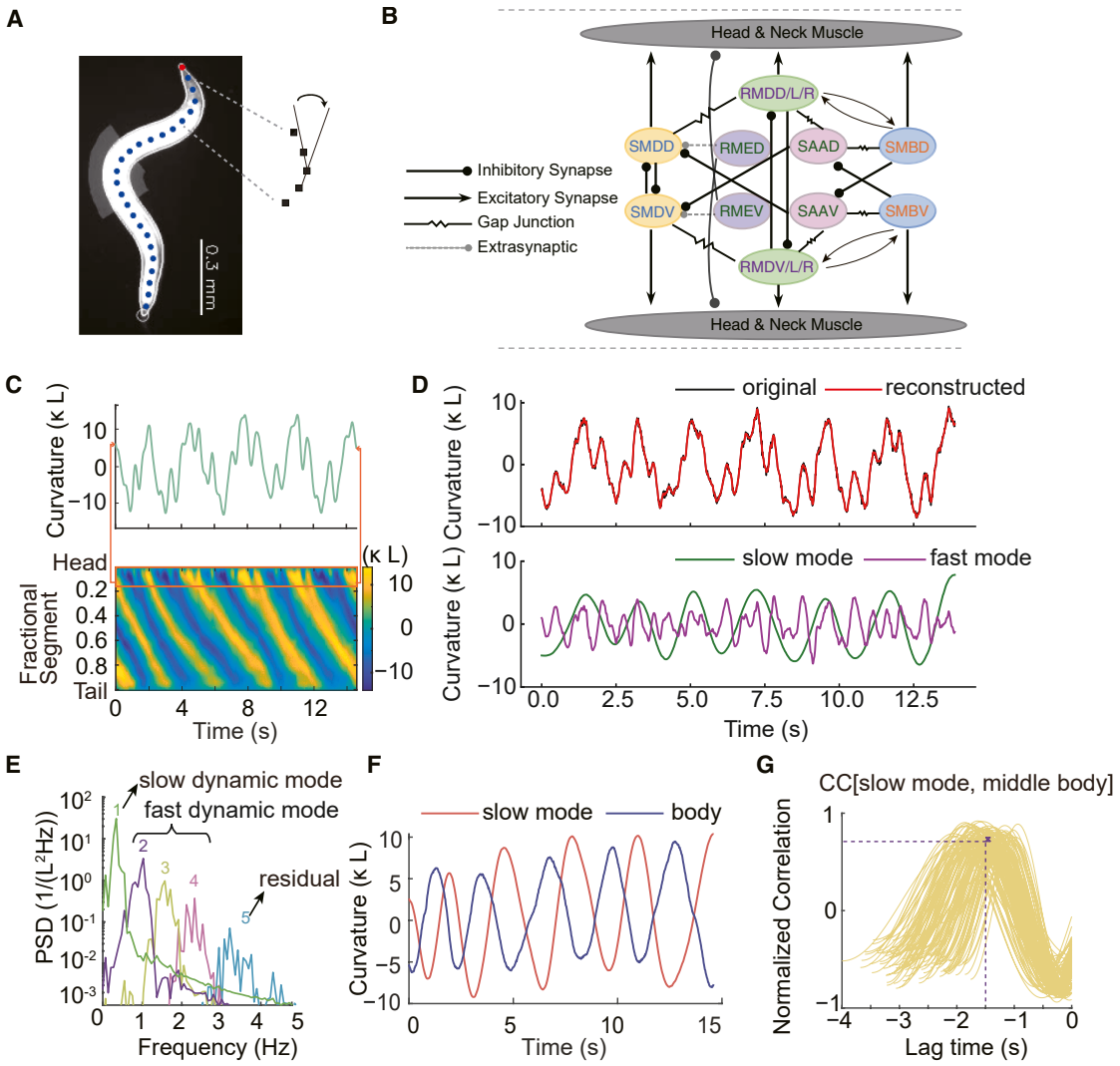

Figure 1. Slow and fast components of head movements

(A) Centerline extraction (blue dotted line) for measuring body curvature along the animal's length.

(B) Schematic of the head motor circuit, consisting of SMD, RMD, SMB, and RME motor neurons and SAA interneurons. Extrasynaptic inhibition was previously reported from RME to SMD.[40]

(C) Representative head curvature and body curvature kymograph of wild-type N2. κ and L denote the curvature variable and the body length, respectively.

(D) Variational mode decomposition (VMD) of a representative head curvature signal. The reconstructed signal is obtained by subtracting the noise mode (mode 5) from the original signal. Slow dynamic mode and fast dynamic mode (slow mode and fast mode for short) correspond to the 1st mode and the summation of modes 2–4, respectively.

(E) Example power spectral density (PSD) of each decomposed mode.

(F) Sample time series of slow mode and middle body curvature (mean curvature of the 45%–60% portion of the body).

(G) Cross-correlation shows high peak correlation between the slow dynamic mode and the middle body curvature.

See also Figure S1.

RMDR innervate both dorsal and ventral muscles.[31,37–39] Additionally, head muscles are innervated by RME (Figure 1B), a class of GABAergic inhibitory motor neurons critical for modulating head-bending amplitude.[40,41] RMDV, RMDL, and SMDV have putative inhibitory connections with their contralateral counterparts—RMDD, RMDR, and SMDD.[31] SMBV and SMBD do not directly connect but are linked indirectly by SAA interneurons (Figure 1B).[31,42] These connectivity patterns, featuring reciprocal inhibition, find parallels in B-type or A-class motor neurons in the *C. elegans* ventral nerve cord[43–45] and, more broadly, in many other motor systems as part of a central pattern generator (CPG).[16,18,46–49] Rhythmic head motion helps establish the body undulation patterns necessary for forward movement[16,45,47] and guides animals toward food sources through a ventral-dorsal bending bias.[30,50–53]

The expansion of the motor hierarchy from a few high-level command neurons[16,36,54] to a larger population of low-level head motor neurons (Figure 1B) raises important questions about their functional organization. Do they have unique or overlapping roles? How do they integrate diverse signals to translate

Please cite this article in press as: Li et al., Multi-timescale motor circuit dynamics underlie adaptive and efficient exploratory behavior, Current Biology (2026), https://doi.org/10.1016/j.cub.2026.05.004

intentions into precise, coordinated, and flexible movements? The circuit motif elucidated by the *C. elegans* connectome[39] and the Ca^{2+} activity correlated with head-bending in certain neurons[29,30,36,40,55,56] do not readily clarify their functional organization. By integrating experimental observations and computational analysis, we demonstrate that three classes of cholinergic motor neurons exert control over distinct aspects of head movements, working in synergy to generate complex, structured dynamics across multiple timescales. We further propose a dual-proprioceptive feedback model that reproduces these movement patterns and demonstrates their role in optimizing movement speed. Together, our findings bridge the gap between the previous phenomenological description of nested head movements[36] and the underlying functional partitioning, suggesting that efficient, adaptive movements emerge from the dynamic interplay within highly interconnected low-level circuits tuned to real-time sensory feedback.

RESULTS

Temporal decomposition of head movements

We recorded *C. elegans* spontaneous crawling behavior at a frame rate of $\sim$90 Hz using dark-field microscopy and computed the head curvature $\kappa(t)$ during forward locomotion by averaging over the first 15% of the body centerline (Figure 1A; STAR Methods). To characterize the dynamics of complex head movements (Figure 1C, top), we applied variational mode decomposition (VMD)[57] to decompose the time-varying signal into modes with increasing central frequencies (Figures 1D, 1E, and S1A). A slower mode exhibits a higher magnitude in the power spectrum (Figure 1E). The sum of modes 1–4 accurately reconstructs head-bending dynamics (Figure 1D). The last mode, which exhibits negligible power and the highest frequency—approximately 1,000 times smaller and 10 times faster than the slowest mode (Figure S1F)—does not represent biologically relevant behavior and was excluded from further analysis.

As illustrated in the spatiotemporal curvature kymograph (Figure 1C, bottom), only the slow rhythmic bending activity of the head propagated posteriorly along the body during *C. elegans* forward locomotion (Figures 1F and S1G). We therefore used VMD to identify the *slow dynamic mode* $\kappa_s(t)$ (mode 1) that has the highest cross-correlation with body bending activity (Figure 1G; STAR Methods). The sum of the remaining modes (modes 2–4) was considered a *fast dynamic mode* $\kappa_f(t)$ intrinsic to head motor activity (Figure 1D, bottom).

Phase-dependent head casts promote shallow turns

Head curvature is sinusoidal, with distinct dips and peaks contributing to the fast dynamic mode. These rapid, intricate movements, dubbed *head casts*,[36] propagate and terminate before the middle body. Our analysis extends this term to include smaller amplitude bends that remain localized within the head region. We pinpoint the location of head casts, characterized by small, rapid bidirectional changes in head curvature (Figure 2A, shaded). These events were identified in the time derivative of the denoised head curvature, since $\dot{\kappa}(t)$ rapidly crosses zero twice, producing a pronounced peak in the time series (Figure 2A, bottom; STAR Methods). Larger amplitude head casts tended to propagate further along the body (Figures S2A and S2B), although most exhibited limited propagating distances (Figure S2C). The occurrence of head casts exhibited a phase-dependent distribution (Figure 2B; STAR Methods) when aligned to the slow dynamic mode. Without loss of generality, we define $\phi = 0$ when the slow-mode curvature κ_s is at its maximum and $\phi = \pi$ when κ_s is at its minimum. Consistent with Kaplan's work,[36] head casts occurred with higher probability when ϕ was in the first or third quadrant (Figure 2C).

We sought to understand how phase-dependent head casts could influence exploratory behaviors on an extended timescale. We observed that head casts are associated with direction changes in *C. elegans* movement (see example trajectory in Figure 2C). We analyzed all head casts within three undulation cycles using a linear regression model to predict changes in the animal's orientation in forward movement (STAR Methods). Linear regression revealed a correlation between head-cast amplitude and changes in movement direction (Figure 2D). These head casts extended the head-bending duration toward one side (Figure 2A), resulting in a dorsal/ventral bias of head-bending (Figure S3A). This led us to hypothesize that this bias translates into changes in running direction. To quantify this bias, we introduced a head bias index calculated as the area under the curve $\kappa(t)$ over three undulation cycles. This bias index showed a significant positive correlation with the change in movement orientation (Figure 2E), as this bias can propagate along the body (Figure S3D).

Beyond the bias in head-bending duration introduced by head casts, another factor contributing to head bias is the head-bending amplitude, as represented by the extrema of the slow-mode signal. Notably, head-bending amplitude showed only weak correlation with head-cast amplitude (Figure 2F), indicating that they encompass distinct characteristics of head movement. To elucidate their respective contributions to directional change, we conducted distinct linear regression analyses assessing (1) head casts in isolation, (2) slow-mode head-bending amplitude in isolation, and (3) both components collectively (Figures S3B and S3C). The variance explained (R^2) from these analyses demonstrated that head casts account for significantly more variance in directional change than slow-mode amplitude alone (Figure 2G), affirming that rapid head movements significantly influence gradual turns beyond mere bias in basic locomotor rhythm. Together, our results highlight the critical role of subtle head movements in steering exploratory behavior.

Different cholinergic motor neuron classes contribute to distinct aspects of head-bending dynamics

We sought to discern the roles of each class of cholinergic motor neuron in head movement using combinatorial optogenetics. With cell-specific promoters, we generated transgenic animals allowing optogenetic ablation of RMD, SMD, and SMB motor neurons either individually or in combination. We quantified changes in head-bending dynamics $\kappa(t)$ (Figures 3A and S4A) by calculating the power of the slow dynamic mode P_s and the fast dynamic mode P_f (Figure 1D; STAR Methods). RMD-ablated animals showed a decrease in the fast dynamic mode contribution, calculated by the power ratio $P_f/(P_s + P_f)$, whereas the contribution of the slow mode grew (Figures 3B and S5C).

Please cite this article in press as: Li et al., Multi-timescale motor circuit dynamics underlie adaptive and efficient exploratory behavior, Current Biology (2026), https://doi.org/10.1016/j.cub.2026.05.004

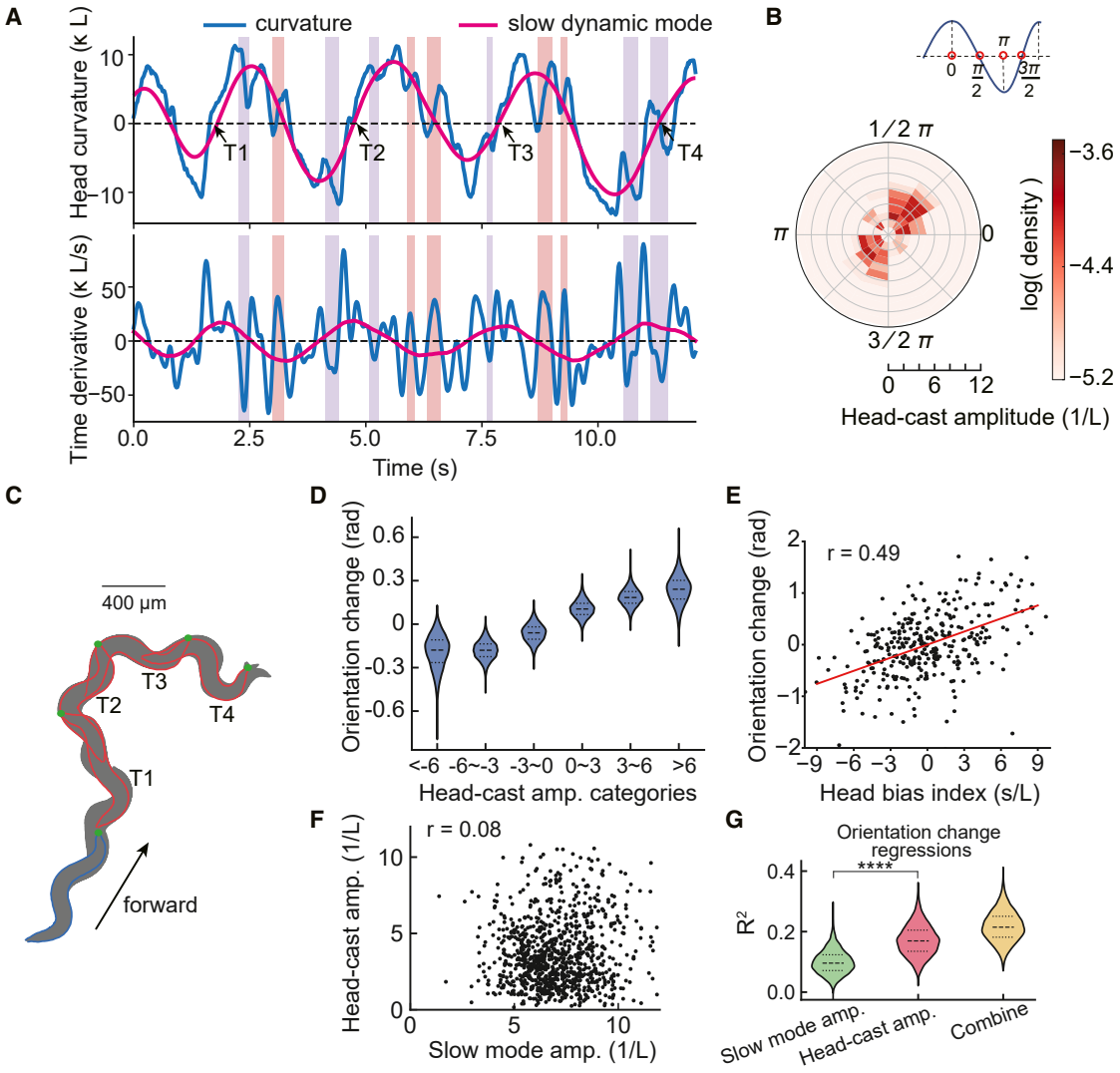

Figure 2. Head casts and their association with gradual directional changes

(A) Top, time series of the head-bending curvature and the corresponding slow dynamic mode. The light red and light blue shaded regions correspond to the dorsal and ventral head casts, respectively. Bottom, time derivatives of the denoised head curvature and slow dynamic mode.

(B) The density map of head casts across stroking amplitude and phase. Phase is defined by the slow dynamic mode, where 0 corresponds to maximum curvature and π to minimum curvature, as illustrated in the upper-right inset. The colormap represents the logarithm of head-cast density, calculated as the total number of head casts within each bin divided by the total trial duration (STAR Methods).

(C) Sequential snapshots of the nematode's posture over three consecutive undulation periods demonstrate a potential link between gradual directional changes and persistent dorsal head casting.

(D) A linear model is employed to assess the impact of head casts at different amplitudes on the directional changes during forward locomotion (STAR Methods). Head casts were grouped into six amplitude categories: < -6, -6 to -3, -3 to 0, 0 to 3, 3 to 6, and >6, with negative levels representing head casts during negative curvature and positive levels during positive curvature. For each three-cycle period, we recorded the orientation change and number of head casts from six amplitude categories. Coefficients were determined using least squares regression. To quantify coefficient uncertainty, the datasets were bootstrapped 10,000 times. The dashed line indicates the median, and the dotted lines indicate the 25th and 75th percentiles.

(E) The total orientation change and dorsoventral bending bias of the head (area under the curvature curve, STAR Methods) were recorded over intervals of three head-bending cycles (black dots). Pearson correlation coefficient r = 0.49, $p = 3.5 \times 10^{-7}$.

(F) The head-cast amplitude showed weak correlation with the slow-mode amplitude. Pearson correlation coefficient r = 0.08, $p = 8 \times 10^{-3}$.

(G) Explained variance of orientation change by linear regressions with respect to the head-bending amplitude, head-cast amplitude, or their combination. Head-cast amplitude explained a higher variance than head-bending amplitude. *t* test, ****$p < 0.0001$.

See also Figures S2, S3, and S13.

Please cite this article in press as: Li et al., Multi-timescale motor circuit dynamics underlie adaptive and efficient exploratory behavior, Current Biology (2026), https://doi.org/10.1016/j.cub.2026.05.004

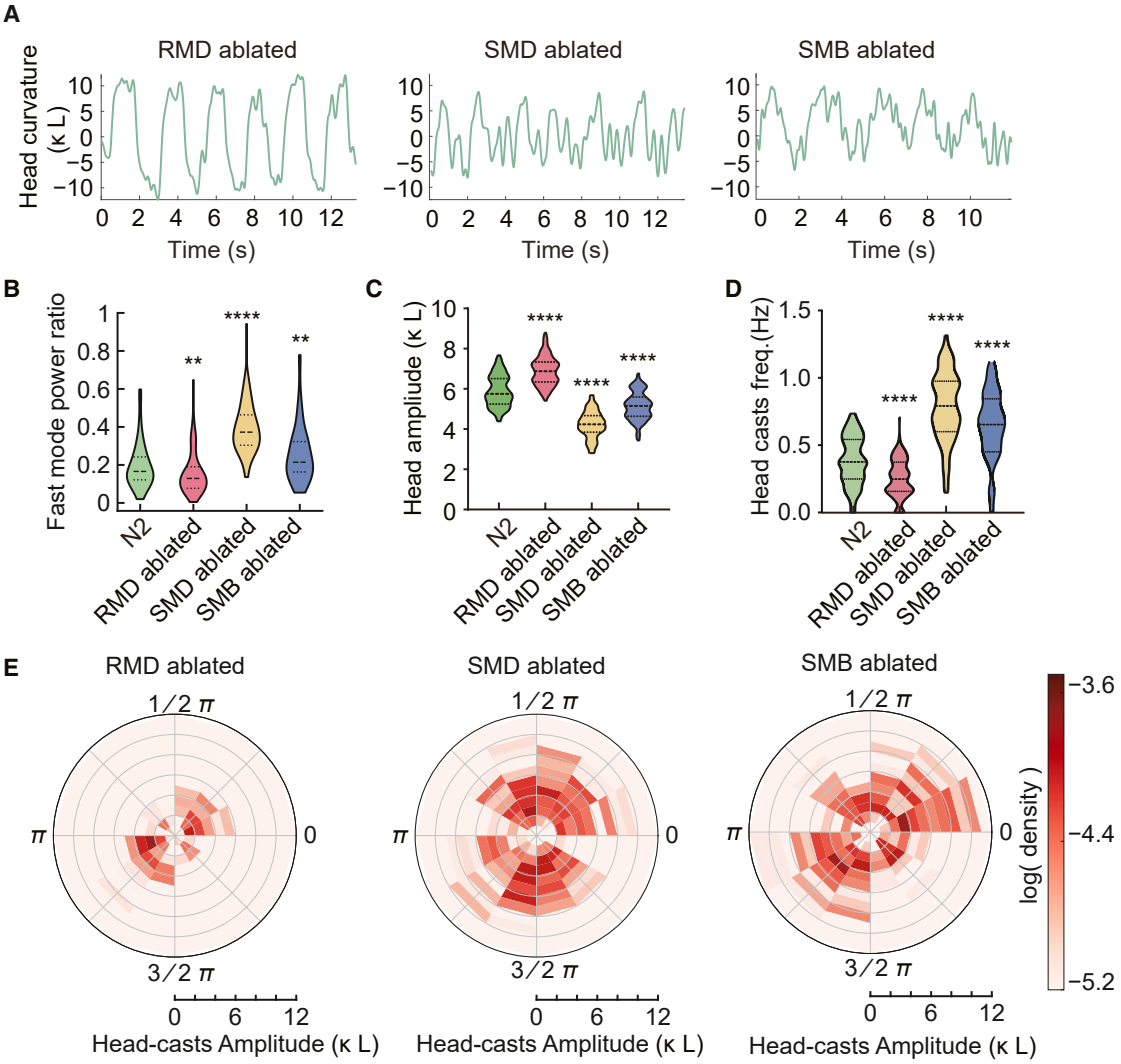

Figure 3. Ablation of different motor neuron classes

(A) Representative head curvatures in head motor neuron-ablated animals.

(B) Power ratio of fast dynamic mode and slow dynamic mode in N2 (n = 108, 18 animals), RMD-ablated animals (n = 138, 19 animals), SMD-ablated animals (n = 101, 15 animals), and SMB-ablated animals (n = 85, 21 animals). n represents the number of episodes of forward movement.

(C) Head-bending amplitude in N2 and motor neuron-ablated animals.

(D) Head cast frequency in each episode of forward movements. The frequency is defined as the number of head casts with a large relative amplitude (STAR Methods) divided by the duration of a forward run.

(E) The density map of head casts over their stroking amplitude and phase in RMD-, SMD-, and SMB-ablated animals.

*p < 0.05, **p < 0.01, ***p < 0.001, ****p < 0.0001, Mann-Whitney U test. All tests are between wild-type and specific cell-type ablated animals. The dashed line in violin plots indicates the median, and the dotted lines indicate the 25th and 75th percentiles.

See also Figures S4–S8 and Video S1.

However, SMD or SMB ablation reversed this trend, diminishing the slow-mode contribution.

Examining the factors causing this power shift, we found that RMD-ablated animals displayed higher head-bending amplitude (Figure 3C; STAR Methods) but lower head-cast frequency (Figure 3D) and lower average head-cast amplitude (Figure 3E, left). On the contrary, SMD- or SMB-ablated animals had a decreased head-bending amplitude (Figure 3C) and elevated head-cast frequency (Figures 3D, S4B, and S5D). These changes aligned with the observed power shifts. Consistently, optogenetic inhibition of SMD suppressed overall head/neck bending (Figures S6A and S6B) and increased the contribution of the fast mode to the head-bending power (Figure S6C). While RMD ablation left the head casts' phase dependence unaltered (Figure 3E, left), SMD or SMB ablation disrupted it, resulting in head casts distributed randomly across all phases of the slow dynamic mode (Figures 3E, middle and right, and S5B).

Furthermore, in SMD- or SMB-ablated animals, the head-body coupling was disrupted. This is evident as the maximum cross-correlation between the slow dynamic mode and the

Please cite this article in press as: Li et al., Multi-timescale motor circuit dynamics underlie adaptive and efficient exploratory behavior, Current Biology (2026), https://doi.org/10.1016/j.cub.2026.05.004

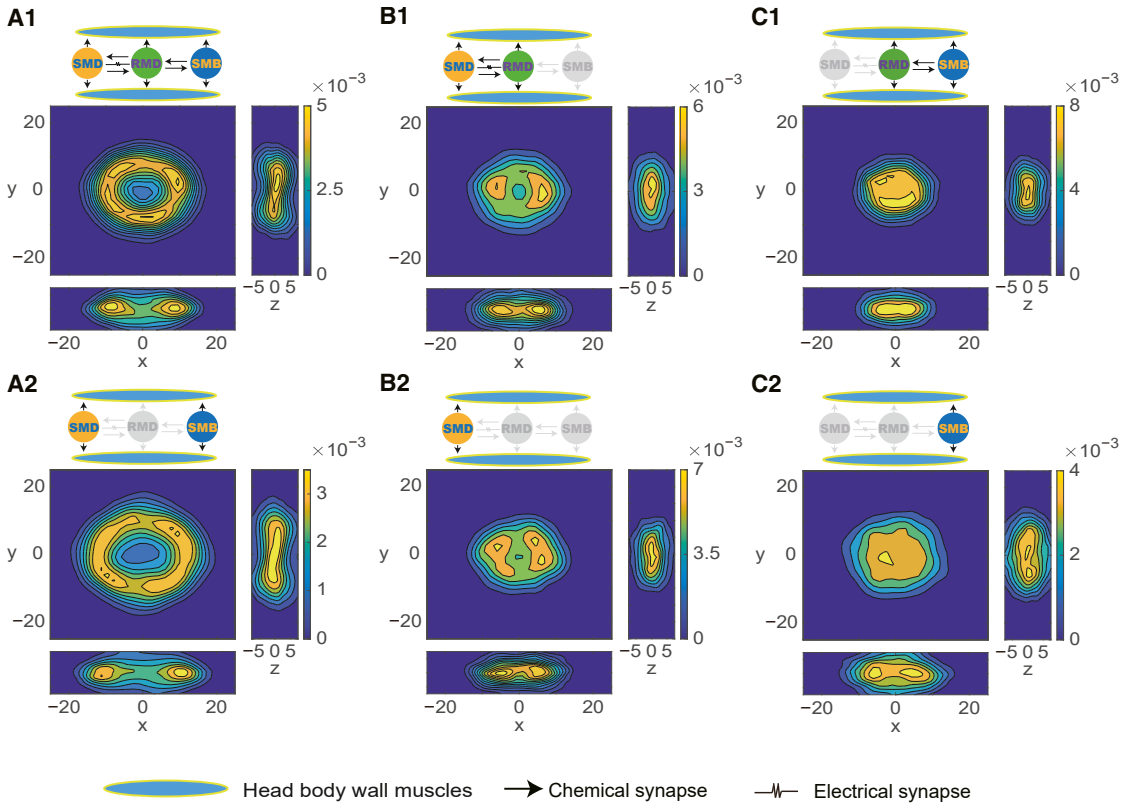

Figure 4. Exploratory head dynamics in an embedding phase space

Each animal's head curvature time series during forward locomotion was embedded into a high-dimensional space with automatically estimated dimensions and delays. The trajectories were then projected onto three principal components (*x*, *y*, and *z* axes), forming a 3D embedding space. Color maps represent trajectory density estimation. Different motor neuron dominance led to varied phase-space density features. At the top of each panel is a schematic of the ablation scheme with gray ellipses representing ablated motor neuron classes. The second row shows animals all with RMD-ablated, and the second and third columns show animals with additional ablation of SMB and SMD, respectively. Topological features vary significantly across columns but show similarities between rows, reflecting dynamic characteristics. (A1 and A2) SMD-SMB dominated control shows a donut-shaped density, suggestive of limit cycle dynamics. (B1 and B2) Animals with SMB-ablated and SMD-dominated bending exhibit two symmetric density clusters, indicating bistable dynamics. (C1 and C2) SMB-dominant control displays a uniform disk-shaped density, a result of chaotic head-bending.

See also Figure S9.

body-bending activity was significantly reduced (Figure S4C). When RMD, SMD, and SMB were co-ablated, rhythmic head-bending was abolished, severely impairing forward but not backward locomotion (Figure S7; Video S1). Sporadic bending events still propagated along the body, likely driven by B-type motor neurons,[16] but without sustained rhythmic head movement, they could not maintain continuous forward undulation. Thus, continuous forward locomotion requires sustained rhythmic bending initiated by the head motor circuit.

Residual head movement varied among triple-ablated animals. In some animals, the head became nearly stationary at a small constant curvature (Figure S7A), consistent with the loss of major oscillatory drives. This phenotype most clearly indicates that RMD, SMD, and SMB together form the main head motor circuit. In others, irregular head movements persisted (Figure S7B) of uncertain origin: they may reflect variable ablation efficiency or inputs from pathways outside our ablation scheme, such as mechanosensitive neurons IL1 and URA, which the connectome identifies as head muscle innervators. The same uncertainty applies to the incomplete loss of head casts after RMD ablation alone (Figure 3E). Optogenetic inhibition of RME[40] or ablation of SAA[42] did not significantly change head-cast dynamics (Figure S8), leaving the identity of any alternative pathways an open question for future investigation.

Phase-space analysis of head-bending dynamics

Next, we applied time-delay embedding to reconstruct the multi-dimensional phase space from the one-dimensional time series $\kappa(t)$ (STAR Methods). According to Takens' theorem, the structure of the reconstructed phase space is topologically equivalent to the original system.[58] This invariance offers a geometric perspective to deepen our understanding of the intricacies of head motor circuit dynamics.

We found that phase trajectories of head movements could be largely embedded in three dimensions. The phase space coordinates are a linear transformation of the time-delayed $\kappa(t)$ and thus are correlated with head curvature and its time derivative (STAR Methods). We used a contour density map and its maximum intensity projection to indicate how often local regions in the phase space were visited (Figure 4). For wild-type

Please cite this article in press as: Li et al., Multi-timescale motor circuit dynamics underlie adaptive and efficient exploratory behavior, Current Biology (2026), https://doi.org/10.1016/j.cub.2026.05.004

animals, these phase-space trajectories appear circular, indicating periodic motion (Figure 4A1). However, irregularity in head movements causes localized scattering, making the overall phase space resemble a donut when visualized using a density plot.

We explored the influence of different motor neuron classes on the topological features of head dynamics by conducting single and combinatorial ablation experiments on three classes of motor neurons. This approach allowed us to observe changes in topology when head movements were governed by one or two classes of motor neurons (Figure 4). When governed predominantly by SMD (with and without RMD in Figures 4B1 and 4B2, respectively), the phase-space density displayed two nearly symmetrical clusters, suggesting bistable dynamics with the head in either a dorsal or ventral bending state. For head movements predominantly governed by SMB (with and without RMD in Figures 4C1 and 4C2, respectively), the ring structure (in Figure 4A1) collapsed, and the phase trajectories spread almost uniformly within a disc. The phase-space center, corresponding to minimal head-bending velocity and amplitude, was visited more frequently than in wild-type animals (also see Figure S9 for SMD and SMB co-ablated animals). Interestingly, RMD ablation expanded the circular density distribution *without* changing its topology (Figure 4A2), whereas SMD or SMB ablation significantly altered the topology. Together, our results suggest that SMD and SMB neurons are major contributors to rhythmic head bending, while RMD neurons aid in fast head casts during the main oscillation.

Differential RMD activity regulates head dynamics in forward movements and reversals

Next, we conducted calcium imaging of RMD neurons (Figure 5A) in freely moving animals (STAR Methods). Our experiments revealed distinct RMD activity patterns during forward and backward locomotion (Figure 5B). RMDD and RMDV neurons showed coordinated activity changes, with calcium levels ramping up simultaneously during the forward-to-reversal transition and decreasing synchronously during the reversal-to-forward transition (Figure 5C). During reversals, the head exhibited regular undulation with significantly reduced head-cast frequency (Figures 5D, 5E, and S11), in agreement with prior findings that foraging was suppressed during escape responses.[34,35] Bilateral RMDD/V coactivation during reversals is consistent with reduced head casting: under our hypothesis, head casting requires asymmetric dorsoventral activation from RMD neurons, whereas bilateral coactivation would stabilize head position.

During forward locomotion, RMDD/V neurons exhibited minimal calcium activity despite vigorous head casting. By contrast, the overlapping RMDL and RMDR neurons showed stronger correlation with curvature than RMDD and RMDV (Figure 5F). We were concerned that slow Ca^{2+} dynamics might lack the temporal resolution to rigorously pinpoint rapid RMD activations driving fast head casts. We therefore used a semi-immobilized condition in which the posterior body was restrained in a microfluidic channel while the anterior part swung slowly in a viscous solution to minimize motion artifacts (Figure S10; STAR Methods). Under these conditions, RMDL and RMDR neurons exhibited distinct, animal-dependent correlation patterns with head curvature (Figures 5G and 5H). In some animals, RMDL and RMDR activity correlated positively and negatively with curvature, respectively, while in others the correlation signs were reversed between RMDL and RMDR, suggesting individual variation in neural control of head movements. Since RMDL and RMDR innervate both dorsal and ventral head muscles despite their left-right anatomical positions,[37] future work should determine whether this variability reflects consistent, animal-specific asymmetries in their synaptic connectivity.

Head casts enhance kinematic efficiency

For long-distance exploration, *C. elegans* must maintain an efficient crawling posture. Previous studies[59,60] suggested that the angle of attack of crawling animals is close to an optimal value for maximum locomotion speed. Here, we provide a theoretical derivation considering the wavelength correction under large undulation amplitudes. Our derivation is based on linear resistive force theory, which effectively links body posture kinematics to locomotion.[61–64] The theory shows that locomotion velocity is given by (STAR Methods)

$$V = \frac{\frac{C_N}{C_L} - 1}{\frac{C_N}{C_L} + \frac{2}{\tan^2(A_a)}} f\lambda_x(b(A_a), k), \qquad \text{(Equation 1)}$$

where C_N is the frictional drag coefficient normal to an infinitesimal segment of the body centerline, C_L is the coefficient tangent to it, and f is the undulation frequency. λ_x is the effective wavelength along the movement direction: it decreases as the wavenumber k and the wave amplitude b increase. b in turn depends on the angle of attack A_a, illustrated in Figure 6A. Equation 1 shows that a small angle of attack increases the slip rate, the ratio between the wave velocity $f\lambda_x$ and the locomotion velocity V, while a large angle reduces the effective wavelength. Both extremes negatively impact speed. Consequently, for a given wavenumber, there is an optimal angle of attack that maximizes the *kinematic efficiency*, defined as V/f. This efficiency measures the distance traveled per undulation cycle and is independent of the undulation frequency (Figure 6B). Our analysis showed that RMD-ablated animals displayed increased head and body curvature (Figures 6A, bottom, and 6C) and the angle of attack (Figure 6D, top), along with decreased locomotion velocity and kinematic efficiency (Figure 6D, middle and bottom).

Given the animal's ability to bend into large curvatures, how does the neural circuit control the amplitude for efficient crawling? What is the optimal head muscle control signal? We predicted that optimal head control should reduce excessive bending amplitude to maintain the angle of attack closer to the optimal value, thereby improving locomotion efficiency. To this end, we assumed the head neural circuit produces a binary input signal that alternates between dorsal and ventral head muscle activation. We simulated head-bending in response to control signals based on a realistic mechanical model and propagated this bending along the body[45,62] (Figure S12A; STAR Methods). We added fast switches in a slow periodic input signal and optimized the pattern to maximize crawling speed (Figures 6E and S12B). The optimal head curvature resembles the observed

Please cite this article in press as: Li et al., Multi-timescale motor circuit dynamics underlie adaptive and efficient exploratory behavior, Current Biology (2026), https://doi.org/10.1016/j.cub.2026.05.004

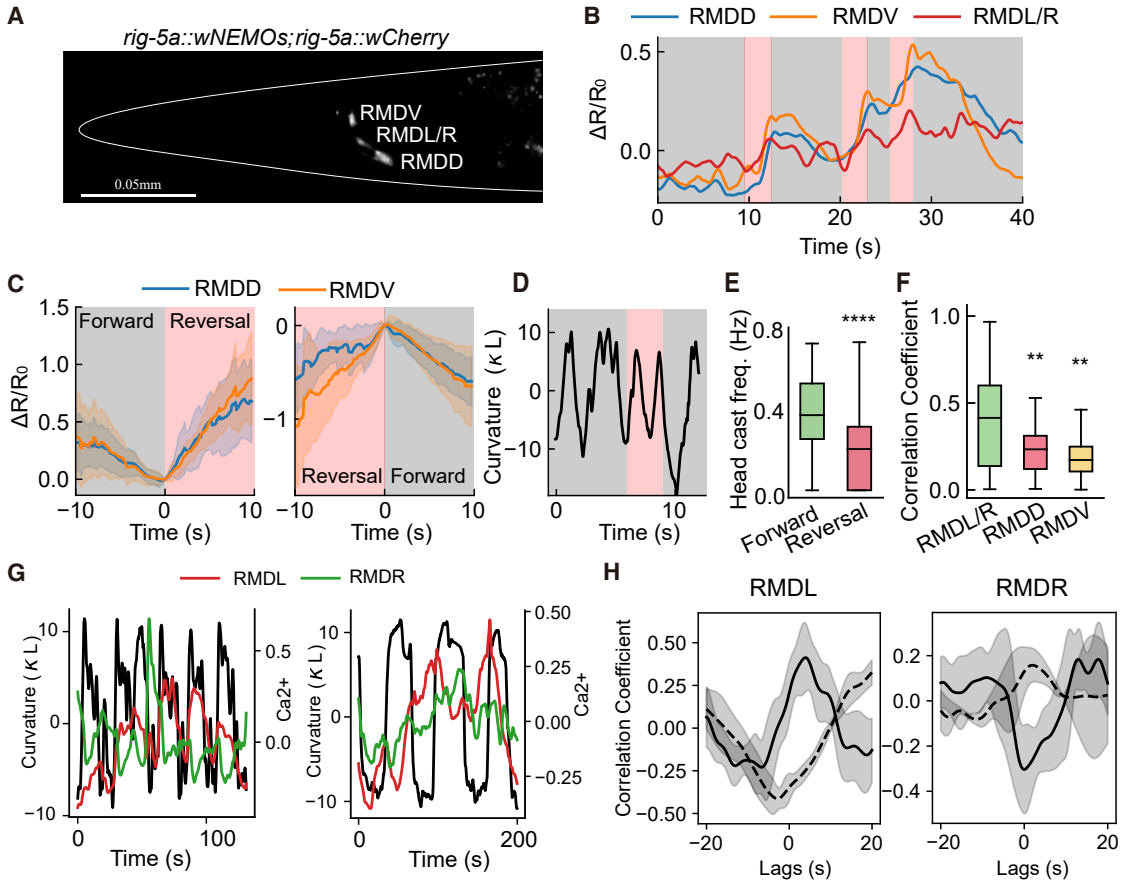

Figure 5. Calcium imaging of RMD neurons

(A) The positions of RMD neurons; the white contour line indicates the head.

(B) Representative RMDD, RMDV, and RMDL/R Ca^{2+} activities in a freely behaving animal, comprising forward movement (gray background) and reversal episodes (red background).

(C) RMDD and RMDV activities ramped up together during forward-to-reversal transitions and decreased synchronously during reversal-to-forward transitions. Number of transitions: $n = 37$, 5 animals. Solid lines represent means of aligned fluorescent signals. At each time point, the mean and SD were computed from all trials that extended beyond that time point, as transition durations varied across events.

(D) Representative head curvature in forward movement (gray background) and reversal (red background).

(E) Animals showed reduced head casting during reversals ($n = 77$, 18 animals) compared with forward episodes ($n = 108$, 18 animals). n represents the number of episodes of forward movement or reversal. **** $p < 0.0001$, Mann-Whitney U test. The box represents the inter-quartile range (25th to 75th percentile), the horizontal line indicates the median, and whiskers extend to 1.5 times the inter-quartile range.

(F) Peak correlation between head-bending curvature and the time derivative of Ca^{2+} activity in RMD subclasses. RMDL/R neurons ($n = 42$ trials from 3 worms) exhibit stronger peak correlation than RMDD ($n = 26$ trials from 3 worms) and RMDV ($n = 26$ trials from 3 worms). **$p < 0.01$, Mann-Whitney U test.

(G) Representative RMDL and RMDR Ca^{2+} activity exhibiting correlation with head curvature. The correlation signs vary across animals (left and right panels show data from two different worms).

(H) Time-lagged correlation between the derivatives of Ca^{2+} activity and head curvature. Solid and dashed lines represent two opposite correlation modes from different animals ($n = 7$ trials from 2 worms and $n = 4$ trials from 2 worms, respectively). In (G) and (H), animals were semi-immobilized, and positive (negative) curvature indicates the dorsal (ventral) side. Panels with shaded areas depict SD.

See also Figures S10 and S11.

phase-specific head casts nested in a slow oscillation (Figure 6E). As predicted by our theory, these simulated head casts reduced both head-bending amplitude and overall body curvature (Figures 6F and S12C) as the bends propagated backward, reducing the angle of attack to near the optimal value of 0.8 (Figures 6B and 6H). This optimized movement pattern increased locomotion velocity by 14% at a period of 2.4 s. Reversing the phase of the fast switches (Figure S12D) led to larger head-bending, similar body-bending curvatures (Figure S12E), and a slight decrease in velocity. Thus, our optimization method clarifies how head casts improve locomotion efficiency and partially explains their timing. The head motor circuit likely imposes additional constraints affecting the phase dependency of head casts.

The head-cast strategy boosts speed by lowering the average angle of attack at frequencies below 0.5 Hz and aligns with the baseline square-wave input above 0.5 Hz (Figures 6G and 6H). Our model thus predicts that when the head oscillation becomes sufficiently fast, head casts will vanish, agreeing with a previous finding.[36] Furthermore, our model simulates a

Please cite this article in press as: Li et al., Multi-timescale motor circuit dynamics underlie adaptive and efficient exploratory behavior, Current Biology (2026), https://doi.org/10.1016/j.cub.2026.05.004

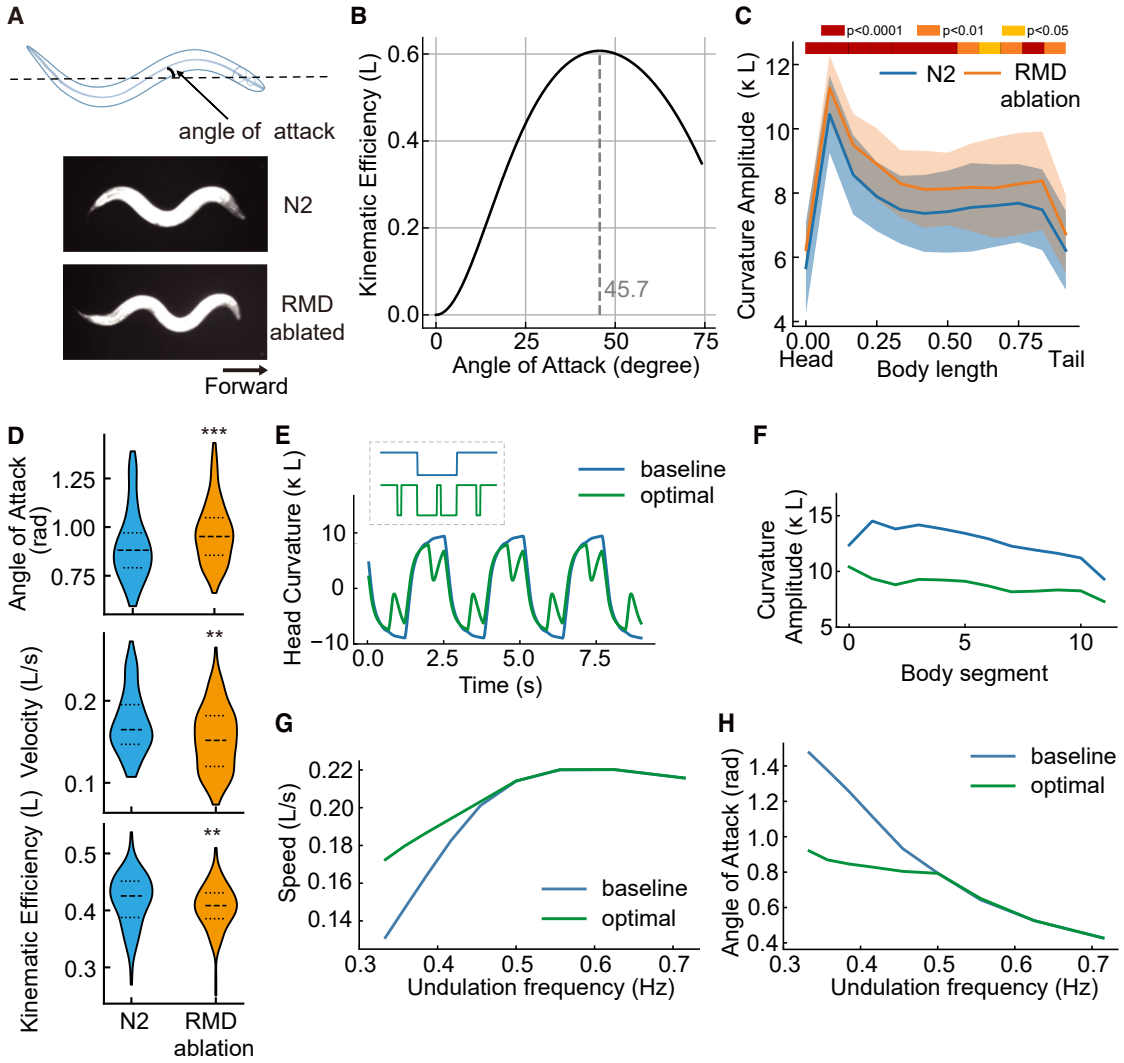

Figure 6. Locomotion efficiency

(A) Angle of attack represents the average angle between the body and movement direction (top). Wild-type N2 (middle) and RMD-ablated animals (bottom) exhibit distinct postures during forward locomotion.

(B) A non-monotonic relationship between kinematic efficiency and angle of attack indicates an optimal angle of attack around 45° for maximum locomotion efficiency. The ratio of drag coefficients $C_N/C_L = 10$ follows recent estimations on agar surface.[65–67]

(C) Optogenetic ablation of RMD neurons ($n = 138$, 19 animals) increased the overall body curvature compared with N2 ($n = 108$, 18 animals). The top heatmap indicates the significance level at different body lengths. Mann-Whitney U test.

(D) RMD-ablated animals ($n = 138$, 19 animals) demonstrate increased angle of attack (top), decreased crawling speed (middle), and reduced kinematic efficiency (bottom) compared with N2 controls ($n = 108$, 18 animals). n denotes the number of episodes of forward run. $^{**}p < 0.01$, $^{***}p < 0.001$, Mann-Whitney U test. The dashed line in violin plots indicates the median, and the dotted lines indicate the 25th and 75th percentiles.

(E) Comparison of head curvatures driven by a baseline square wave input and the optimized head muscle input (inset, dashed box). The head input period is fixed at 2.4 s.

(F) Curvature along the body shows an overall decrease following the optimized head input from (E).

(G) Locomotion speed under baseline and optimized head input across various undulation frequencies.

(H) Similar to (G), but for angle of attack.

See also Figure S12.

reduction in muscle energy expenditure due to decreased overall curvature (Figure S12F). Together, our results suggest that by optimizing head muscle input in our neuromechanical model, phase-specific head casts effectively control crawling posture, maximizing velocity and minimizing energy use during locomotion.

A bend-sensitive feedback model captures slow and fast dynamics

We asked whether the observed fast and slow head-bending activity could be reproduced by a minimal model consistent with known anatomical and functional data. Our ablation experiments demonstrated the synergistic role of SMD and SMB as a

Please cite this article in press as: Li et al., Multi-timescale motor circuit dynamics underlie adaptive and efficient exploratory behavior, Current Biology (2026), https://doi.org/10.1016/j.cub.2026.05.004

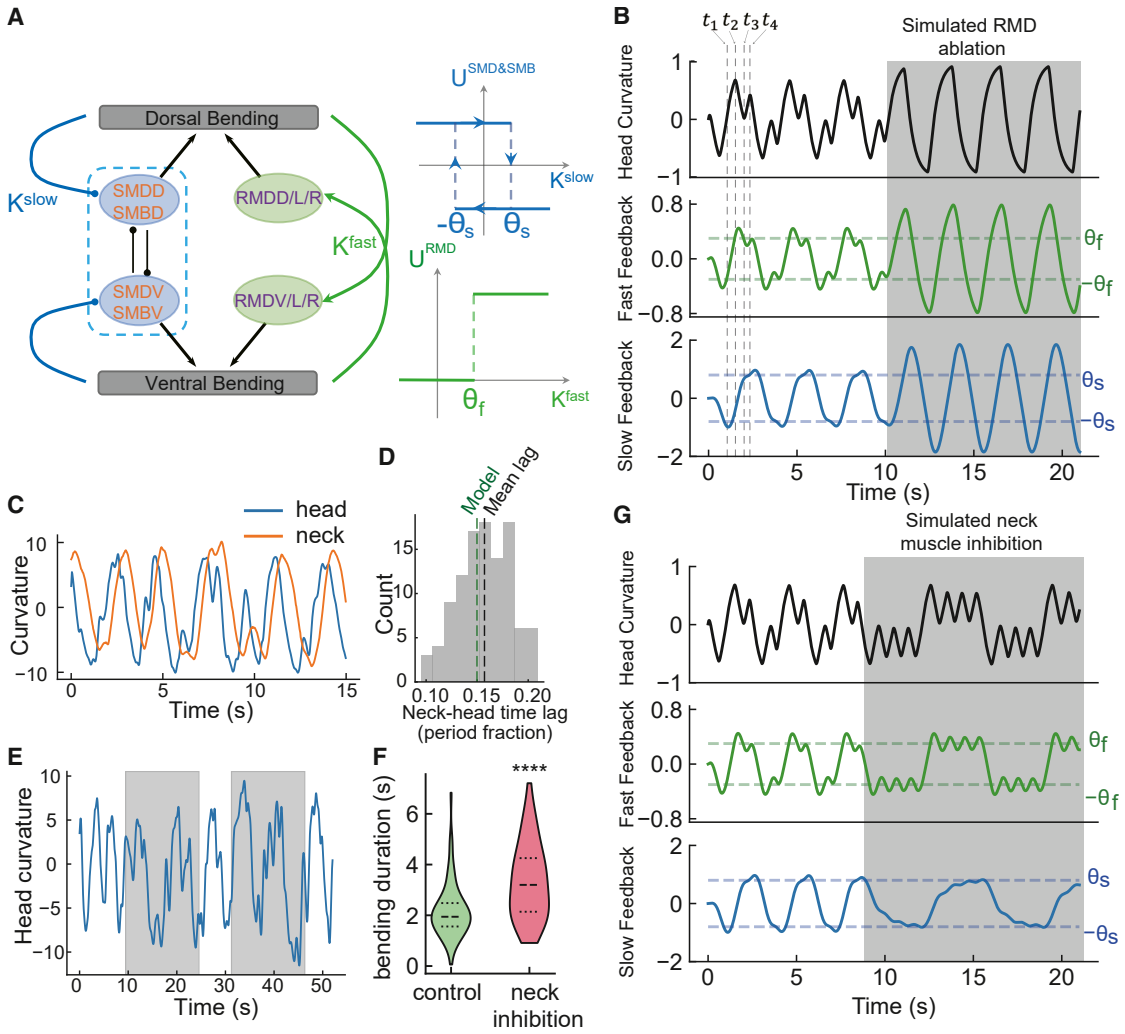

Figure 7. A circuit model captures the fast and slow dynamic modes

(A) Schematic of the model circuit and the bistable dynamics of its elements. SMD and SMB motor neurons on the same side operate as one functional unit and receive a slow integration of the head curvature K^{slow} as feedback. The mutually inhibiting dorsal-ventral units were posited to operate in a bistable regime and have a hysteresis curve in the input-voltage relation (middle). RMDD/L/R and RMDV/L/R correspond to dorsal and ventral head muscles innervated by RMD neurons, respectively. Their activation levels are switched by a fast integration of head curvature K^{fast} (right).

(B) Representative trajectories of head curvature, fast feedback, and slow feedback. Dashed lines indicate the four different circuit states: t_1: dorsal SMD-SMB unit was activated. t_2: the fast curvature feedback activated RMDV/L/R, generating an opposite muscle torque. t_3: decreased fast feedback shut RMDV/L/R down. t_4: slow curvature feedback switched the slow oscillatory module to ventral outputting. The shaded area simulated RMD ablation, which showed increased head-bending amplitude due to the lack of fast feedback.

(C) Representative head (0%–15% body length) and neck (15%–30% body length) curvature from wild-type animals.

(D) Histogram of time lags between head and neck curvature in N2 animals (n = 108, 18 animals). The mean time lag was 0.16 undulation periods, consistent with the time lag between head curvature and surrogate posterior curvature in the model (0.15 periods).

(E) Representative head curvature during optogenetic neck inhibition. Illumination (shaded area) induces extended bending toward both sides.

(F) Significant increase in time spent bending toward both sides during neck inhibition (n = 50, 2 animals). For control: n = 75, 2 animals; $p = 1.1 \times 10^{-5}$, Mann-Whitney U test. The dashed line indicates the median, and the dotted lines indicate the 25th and 75th percentiles.

(G) Simulated neck inhibition (shaded area) showed excessive head casts and extended bending duration.

dominant slow oscillatory module and the role of RMD in generating head casts. Direct or indirect cross-inhibition between contralateral SMD/SMB neurons, along with our ablation studies, suggests that the slow oscillator operates through bistable switching. We modeled SMDD and SMBD as one dorsal unit and SMDV and SMBV as one ventral unit (Figure 7A, left), activating dorsal and ventral muscles, respectively. Both units exhibit bistable dynamics, modeled as a hysteresis curve[68] (Figure 7A, right). SMD and SMB, with posterior sublateral processes, are hypothesized to sense posterior curvature. Thus, our model includes proprioceptive feedback from neck bending to the slow oscillatory module, acting as slow integration of head curvature, captured by K^{slow} (Figure 7A, left; STAR Methods).

Please cite this article in press as: Li et al., Multi-timescale motor circuit dynamics underlie adaptive and efficient exploratory behavior, Current Biology (2026), https://doi.org/10.1016/j.cub.2026.05.004

On the fast timescale, earlier electrophysiological measurements[69] suggest that RMD motor neurons operate in a bistable state. As upstream mechanosensitive neurons (e.g., URY, IL1, OLQ, and CEP) may sense head pressure,[31–33] we hypothesize that RMD neurons, grouped by muscle innervation—RMDD/L/R (dorsal-innervating) and RMDV/L/R (ventral-innervating)—receive rapid feedback from head curvature, captured by K^{fast}, toggling transient neural activity (Figure 7A, right). Our model thus includes two parallel neuronal groups and a dual-feedback system that integrates head curvature over two distinct timescales.

When the head bends dorsally (positive curvature, Figure 7B, t_1), fast feedback follows the head curvature and activates the RMD neurons innervating ventral muscles at the threshold θ_f (at t_2 in Figure 7B), producing opposite muscle torque and reducing head curvature. The fast feedback signal then drops below θ_f, turning off the RMD neurons (at t_3 in Figure 7B). However, input to dorsal muscles from the slow oscillatory module persists, increasing dorsal bending. Therefore, fast negative feedback could generate phase-specific head casts. The activity of the slow oscillatory module is regulated by a low-pass filter of the head curvature K^{slow} that mimics neck movement. Indeed, the observed phase lag between head and neck curvature in real animals closely matches the lag between head curvature and surrogate posterior curvature in our model (Figures 7C and 7D; STAR Methods). Sustained bending enhances this negative feedback until it reaches the threshold θ_s, at which point the neuronal state switches from dorsal to ventral activation (at t_4 in Figure 7B), producing the slow dynamic mode. Ablating RMD neurons in simulations by removing their muscle input showed a similar increase in bending amplitude as seen in experiments (Figures 3A and 7B).

A key prediction of the model is that feedback originating from neck bending plays a crucial role in defining the slow dynamic mode. To test this, we reduced the neck curvature by optogenetically inhibiting the neck muscles. Upon inhibition, the head bent to one side for a long time, significantly increasing the duration on both sides (Figures 7E and 7F). This observation can be captured by our model: reducing the slow feedback signal amplitude led to longer accumulation and thus extended the period of the slow oscillator (Figure 7G), consistent with the persistent head-bending state observed in experiments.

DISCUSSION

Bilaterians have thrived evolutionarily because their bilaterally symmetrical body plan supports sophisticated directed movement.[70] Such movements involve efficient forward propulsion and controlled turning, with head movements being key to both maintaining forward speed and steering in animals like fish[71] and snakes.[72] The *C. elegans* head motor circuit, a minimal system capable of generating highly adaptable movements, demonstrates motor patterns with a structured composition where rapid, phase-specific head casts are nested within slower, rhythmic head oscillations.[36] Here, by combining experimental manipulations and neuromechanical modeling, we demonstrate that these intrinsic dynamics emerge from interactions among three classes of cholinergic motor neurons, each serving a distinct function. SMD and SMB neurons together generate robust, limit-cycle-like slow head oscillations, while RMD neurons modulate head casts without modifying the overall topology of the dynamics (Figure 4).

State-dependent control and the scaffolding of adaptive behavior

During reversals, head-bending displays increased regularity with notably fewer head casts (Figures 5E and S11), confirming a previous observation.[35] This shift coincides with simultaneous activation of both RMDD and RMDV neurons, providing symmetric dorsoventral muscle inputs. This contrasts with the complex and head-bending correlated activity in RMDL and RMDR neurons (Figures 5G and 5H) and the unilateral input that our computational model hypothesizes to drive head casting during forward movement.

These findings collectively suggest that coordinated activity of SMD, SMB, and RMD neurons underpins a hierarchical organization of head movements. Interestingly, in gap-junction-deficient mutants (*unc-7* and *unc-9*), head casts occur randomly across locomotion phases (Figure S13), underscoring the importance of intercellular coupling in maintaining phase-dependent coordination. The regularization of dynamics during the reversal state suggests a *shift* toward more stereotyped, feedforward descending control, with RMDD/V synchronization acting as a landmark for motor state transitions.

This modular architecture—where slow oscillations provide a scaffold for context-dependent, faster maneuvers—exemplifies a general principle for balancing robustness and flexibility in motor systems. For example, in multi-legged animals, this manifests as the difference between slow postural control and fast dynamic adjustments.[73,74] The slow, basic process of postural control, which continuously maintains balance, is analogous to the slow, rhythmic movements orchestrated by SMD/SMB neurons. Superimposed on these slow rhythms are faster, sensory-driven adjustments, much like the function of RMD neurons in mediating fast head casts.

A similar organizational principle operates in the respiratory system, where bursts are the primary slow rhythmic outputs that drive the basic respiratory cycle, providing the fundamental scaffold for breathing. Burstlets[75,76] in the bilaterally distributed brainstem structure called the preBötzinger complex, on the other hand, are smaller, faster bursts of activity that are superimposed on the main burst. These burstlets do not directly trigger motor outputs but allow dynamic, rapid adjustments to the breathing pattern. Such multi-timescale organization allows many systems to maintain a stable baseline while retaining flexibility to adapt quickly to changing internal or external conditions.

Head casting as a motor grammar for flexible exploratory behavior

What is the behavioral significance of head casts in *C. elegans*? These rapid head movements propagate posteriorly along the body for a limited distance, an observation that remains consistent despite differences in the parameters used to define the spatial extent of head curvature between previous work[36] and ours (Figures S2C and S2E; STAR Methods). Here, we discovered a significant correlation between head casts and animal reorientation, along with a causal relationship between dorsal-ventral bending biases in the head and the middle body, where head bends propagate, linking intricate head movements with

the animal's overall turning behavior. Prior research has shown that the curved paths during weathervane behavior stem from asymmetric dorsoventral modulation of head bending.[77] Theoretical and empirical studies suggest this occurs through differential gain modulation of contralateral head motor neurons in response to a chemical gradient.[51,78,79] We propose head casting as a new navigation strategy, achieved by a dorsoventrally asymmetric number of head casts. In essence, adjusting the timing and amplitude of head casts alters the phase and amplitude of the slow oscillatory module. Future research should confirm the role of head casting in reorientation amid sensory signal gradients and other complex environments.

The head is crucial for initiating and leading forward movement, with its undulation necessary for coordinating body waves and generating propulsion. Head and body movements are closely coupled, potentially through directional proprioceptive coupling,[45] resulting in a strong correlation of amplitude and entrainment of the undulation frequency.[16,47] Here, we show that RMD, SMD, and SMB neurons form key components of the head motor circuit supporting rhythmic head bending. When all three motor neuron classes were ablated, *C. elegans* rarely sustained forward undulatory waves (Video S1) and mostly moved backward. These observations are consistent with the recent finding[42] that the head motor circuit provides negative feedback to the motor control center during reversals. Furthermore, using a computational model, we discovered that control signals for head casts emerged from optimizing movement velocity. The model predicts that animals tune their overall bending amplitude near an optimal value for efficiency. This explains the ubiquity of head casts in the locomotion of *C. elegans*: the animal employs this strategy to dynamically adjust their posture, keeping it optimized for efficient long-distance exploration.

Although our experiments were conducted in a controlled environment to isolate core circuit functions, our findings provide a mechanistic explanation for how adaptive and exploratory behaviors can be generated in complex settings. In particular, the dual-proprioceptive feedback model provides a general control scheme for maintaining internal stability while permitting adaptive flexibility—a core requirement for navigating variable and unpredictable terrains. The ability to execute a rapid head cast without compromising the integrity of the underlying rhythmic gait is precisely the kind of motor grammar needed to integrate new sensory information on the move. This is the essence of behavioral adaptability: the seamless integration of a discrete, goal-directed action with an ongoing, automated pattern. Thus, while we measure motor efficiency as optimized speed, the deeper significance of our results lies in revealing this underlying algorithm for flexible control. This dynamic interplay between a stable rhythm generator and discrete steering commands is what allows the animal to make a continuous stream of minor corrections and major reorientations underlying efficient exploration, transitioning seamlessly from long-range traversal to local examination.

A biophysical model for dual-timescale control: Integrating feedback and neuronal nonlinearity

Current literature has extensively documented the bidirectional mapping between brain activity and behavior. Using whole-brain imaging in *C. elegans*, Kaplan and colleagues offered mechanistic insight into nested neuronal dynamics that coordinate hierarchical behavior across multiple timescales.[36] Conversely, Atanas et al. revealed how individual neuron activity encodes specific behavioral states.[80] A critical gap persists between identifying these global representations and understanding how they are physically instantiated to drive movements. Here, we propose a model for *C. elegans* head movements, where slow and fast dynamic modes emerge from the interplay between dual-timescale negative proprioceptive feedback and the bistable dynamics of circuit components. Fast feedback to the RMD neurons likely comes from diverse mechanosensitive neurons, such as URY, IL1, OLQ, and CEP.[31–33] Individual RMD neurons have a bistable membrane potential,[69] a mode that allows nonlinear responses to mechanosensitive inputs. The neck and body act as low-pass filters, delaying, and smoothing head movement. The posterior sublateral extensions of SMD and SMB neurons could act as stretch receptors, detecting the posterior curvature and providing slow feedback. This circuit modulates bistable state transitions of the slow oscillatory module to generate a slow dynamic mode. Together, rapid local feedback, delayed slow feedback, and neuronal nonlinearity shape the dual oscillatory head movements and work collectively to optimize locomotion efficiency.

RESOURCE AVAILABILITY

Lead contact

Further information and requests for resources should be directed to and will be fulfilled by the lead contact, Heng Zhang (heng.zhang@stu.pku.edu.cn).

Materials availability

Resources, constructs, and strains from this study are available from Quan Wen (qwen@ustc.edu.cn) upon request.

Data and code availability

- All data reported in this paper will be shared by the lead contact upon request.
- Custom Python analysis code has been deposited at 10.5281/zenodo.19794971 and is publicly available as of the date of publication.
- Any additional information required to reanalyze the data reported in this work is available from the lead contact upon request.

ACKNOWLEDGMENTS

The authors appreciate helpful discussions with Dmitri Chklovskii, Shangbang Gao, Yuichi Iino, Mei Zhen, and Manuel Zimmer. P.L., H.Z., J.W., Y.S., L.T., and Q.W. were partially supported by the National Natural Science Foundation of China through the Major International (Regional) Joint Research Project (32020103007). N2 strains were provided by the CGC, which is funded by NIH Office of Research Infrastructure Programs (P40 OD010440).

AUTHOR CONTRIBUTIONS

P.L. designed and carried out most experiments and performed preliminary analysis of the data. H.Z. analyzed all behavioral data, developed the circuit model, conceptualized and developed the efficient exploration model, and wrote the original manuscript and its revision. J.W. performed Ca^{2+} imaging and analyzed the activity data, contributing to the revision. Y.S. contributed to the circuit model. L.T. and Q.W. conceptualized the project, designed the experiments, performed the analysis, contributed to modeling, and wrote the original manuscript and its revision.

DECLARATION OF INTERESTS

The authors declare no competing interests.

STAR★METHODS

Detailed methods are provided in the online version of this paper and include the following:

- KEY RESOURCES TABLE
- EXPERIMENTAL MODEL AND STUDY PARTICIPANT DETAILS
- METHOD DETAILS
  - *C. elegans* strains
  - Molecular biology
  - Behaviour recording
  - Optogenetic ablation
  - Optogenetics
  - Behavioural analysis
  - Calcium imaging
  - Circuit Model
  - Neuro-mechanical Model
  - Phase space reconstruction
  - Optimal angle of attack for maximum locomotion speed
- QUANTIFICATION AND STATISTICAL ANALYSIS
  - Kinematic analysis of head movements
  - Variational mode decomposition
  - Head-cast analysis
  - Linear regression to relate head cast and turning angle
  - Statistical test

SUPPLEMENTAL INFORMATION

Supplemental information can be found online at https://doi.org/10.1016/j.cub.2026.05.004.

Received: May 21, 2025
Revised: September 25, 2025
Accepted: May 5, 2026

REFERENCES

1. Todorov, E., and Jordan, M.I. (2002). Optimal feedback control as a theory of motor coordination. Nat. Neurosci. *5*, 1226–1235. https://doi.org/10.1038/nn963.
2. Abram, S.J., Poggensee, K.L., Sánchez, N., Simha, S.N., Finley, J.M., Collins, S.H., and Donelan, J.M. (2022). General variability leads to specific adaptation toward optimal movement policies. Curr. Biol. *32*, 2222–2232. https://doi.org/10.1016/j.cub.2022.04.015.
3. Dhawale, A.K., Smith, M.A., and Ölveczky, B.P. (2017). The Role of Variability in Motor Learning. Annu. Rev. Neurosci. *40*, 479–498. https://doi.org/10.1146/annurev-neuro-072116-031548.
4. Yang, H.H., Brezovec, B.E., Serratosa Capdevila, L., Vanderbeck, Q.X., Adachi, A., Mann, R.S., and Wilson, R.I. (2024). Fine-grained descending control of steering in walking Drosophila. Cell *187*, 6290–6308. https://doi.org/10.1016/j.cell.2024.08.033.
5. Thiele, T.R., Donovan, J.C., and Baier, H. (2014). Descending control of swim posture by a midbrain nucleus in zebrafish. Neuron *83*, 679–691. https://doi.org/10.1016/j.neuron.2014.04.018.
6. Bouvier, J., Caggiano, V., Leiras, R., Caldeira, V., Bellardita, C., Balueva, K., Fuchs, A., and Kiehn, O. (2015). Descending Command Neurons in the Brainstem that Halt Locomotion. Cell *163*, 1191–1203. https://doi.org/10.1016/j.cell.2015.10.074.
7. Ruder, L., Takeoka, A., and Arber, S. (2016). Long-Distance Descending Spinal Neurons Ensure Quadrupedal Locomotor Stability. Neuron *92*, 1063–1078. https://doi.org/10.1016/j.neuron.2016.10.032.
8. Brecht, M., Schneider, M., Sakmann, B., and Margrie, T.W. (2004). Whisker movements evoked by stimulation of single pyramidal cells in rat motor cortex. Nature *427*, 704–710. https://doi.org/10.1038/nature02266.
9. Churchland, M.M., Cunningham, J.P., Kaufman, M.T., Foster, J.D., Nuyujukian, P., Ryu, S.I., and Shenoy, K.V. (2012). Neural population dynamics during reaching. Nature *487*, 51–56. https://doi.org/10.1038/nature11129.
10. Brownstone, R.M., Bui, T.V., and Stifani, N. (2015). Spinal circuits for motor learning. Curr. Opin. Neurobiol. *33*, 166–173. https://doi.org/10.1016/j.conb.2015.04.007.
11. Johnson, M.D., and Heckman, C.J. (2014). Gain control mechanisms in spinal motoneurons. Front. Neural Circuits *8*, 81. https://doi.org/10.3389/fncir.2014.00081.
12. Mazzucato, L. (2022). Neural Mechanisms Underlying the Temporal Organization of Naturalistic Animal Behavior. eLife *11*, e76577. https://doi.org/10.7554/eLife.76577.
13. Susilaradeya, D., Xu, W., Hall, T.M., Galán, F., Alter, K., and Jackson, A. (2019). Extrinsic and intrinsic dynamics in movement intermittency. eLife *8*, e40145. https://doi.org/10.7554/eLife.40145.
14. Kalidindi, H.T., Cross, K.P., Lillicrap, T.P., Omrani, M., Falotico, E., Sabes, P.N., and Scott, S.H. (2021). Rotational dynamics in motor cortex are consistent with a feedback controller. eLife *10*, e67256. https://doi.org/10.7554/eLife.67256.
15. Marder, E., and Bucher, D. (2001). Central pattern generators and the control of rhythmic movements. Curr. Biol. *11*, R986–R996. https://doi.org/10.1016/S0960-9822(01)00581-4.
16. Xu, T., Huo, J., Shao, S., Po, M., Kawano, T., Lu, Y., Wu, M., Zhen, M., and Wen, Q. (2018). Descending pathway facilitates undulatory wave propagation in Caenorhabditis elegans through gap junctions. Proc. Natl. Acad. Sci. USA *115*, E4493–E4502. https://doi.org/10.1073/pnas.1717022115.
17. Hahnloser, R.H.R., Kozhevnikov, A.A., and Fee, M.S. (2002). An Ultra-Sparse Code Underlies the Generation of Neural Sequences in a Songbird. Nature *419*, 65–70. https://doi.org/10.1038/nature00974.
18. Kiehn, O. (2006). Locomotor circuits in the mammalian spinal cord. Annu. Rev. Neurosci. *29*, 279–306. https://doi.org/10.1146/annurev.neuro.29.051605.112910.
19. Dagenais, P., Hensman, S., Haechler, V., and Milinkovitch, M.C. (2021). Elephants evolved strategies reducing the biomechanical complexity of their trunk. Curr. Biol. *31*, 4727–4737. https://doi.org/10.1016/j.cub.2021.08.029.
20. Zhu, S., Lakshminarasimhan, K.J., Arfaei, N., and Angelaki, D.E. (2022). Eye movements reveal spatiotemporal dynamics of visually-informed planning in navigation. eLife *11*, e73097. https://doi.org/10.7554/eLife.73097.
21. Berg, H.C. (1993). Random Walks in Biology (Princeton University Press).
22. Pierce-Shimomura, J.T., Morse, T.M., and Lockery, S.R. (1999). The fundamental role of pirouettes in Caenorhabditis elegans chemotaxis. J. Neurosci. *19*, 9557–9569. https://doi.org/10.1523/JNEUROSCI.19-21-09557.1999.
23. Iino, Y., and Yoshida, K. (2009). Parallel use of two behavioral mechanisms for chemotaxis in Caenorhabditis elegans. J. Neurosci. *29*, 5370–5380. https://doi.org/10.1523/JNEUROSCI.3633-08.2009.
24. Stephens, G.J., Johnson-Kerner, B., Bialek, W., and Ryu, W.S. (2010). From Modes to Movement in the Behavior of Caenorhabditis elegans. PLoS One *5*, e13914. https://doi.org/10.1371/journal.pone.0013914.
25. Vergassola, M., Villermaux, E., and Shraiman, B.I. (2007). 'Infotaxis' as a strategy for searching without gradients. Nature *445*, 406–409. https://doi.org/10.1038/nature05464.
26. Calhoun, A.J., Chalasani, S.H., and Sharpee, T.O. (2014). Maximally informative foraging by Caenorhabditis elegans. eLife *3*, e04220. https://doi.org/10.7554/eLife.04220.
27. Flavell, S.W., Pokala, N., Macosko, E.Z., Albrecht, D.R., Larsch, J., and Bargmann, C.I. (2013). Serotonin and the neuropeptide PDF initiate and extend opposing behavioral states in C. elegans. Cell *154*, 1023–1035. https://doi.org/10.1016/j.cell.2013.08.001.

28. Izquierdo, E.J., and Lockery, S.R. (2010). Evolution and analysis of minimal neural circuits for klinotaxis in Caenorhabditis elegans. J. Neurosci. *30*, 12908–12917. https://doi.org/10.1523/JNEUROSCI.2606-10.2010.

29. Yeon, J., Kim, J., Kim, D.Y., Kim, H., Kim, J., Du, E.J., Kang, K., Lim, H.H., Moon, D., and Kim, K. (2018). A sensory-motor neuron type mediates proprioceptive coordination of steering in C. elegans via two TRPC channels. PLoS Biol. *16*, e2004929. https://doi.org/10.1371/journal.pbio.2004929.

30. Hendricks, M., Ha, H., Maffey, N., and Zhang, Y. (2012). Compartmentalized calcium dynamics in a C. elegans interneuron encode head movement. Nature *487*, 99–103. https://doi.org/10.1038/nature11081.

31. White, J. (2018). Clues to basis of exploratory behaviour of the C. elegans snout from head somatotropy. Philos. Trans. R. Soc. Lond., B Biol. Sci. *373*, 20170367. https://doi.org/10.1098/rstb.2017.0367.

32. Hart, A.C., Sims, S., and Kaplan, J.M. (1995). Synaptic code for sensory modalities revealed by C. elegans GLR-1 glutamate receptor. Nature *378*, 82–85. https://doi.org/10.1038/378082a0.

33. Kindt, K.S., Viswanath, V., Macpherson, L., Quast, K., Hu, H., Patapoutian, A., and Schafer, W.R. (2007). Caenorhabditis elegans TRPA-1 functions in mechanosensation. Nat. Neurosci. *10*, 568–577. https://doi.org/10.1038/nn1886.

34. Alkema, M.J., Hunter-Ensor, M., Ringstad, N., and Horvitz, H.R. (2005). Tyramine Functions independently of octopamine in the Caenorhabditis elegans nervous system. Neuron *46*, 247–260. https://doi.org/10.1016/j.neuron.2005.02.024.

35. Pirri, J.K., McPherson, A.D., Donnelly, J.L., Francis, M.M., and Alkema, M.J. (2009). A Tyramine-Gated Chloride Channel Coordinates Distinct Motor Programs of a Caenorhabditis elegans Escape Response. Neuron *62*, 526–538. https://doi.org/10.1016/j.neuron.2009.04.013.

36. Kaplan, H.S., Salazar Thula, O., Khoss, N., and Zimmer, M. (2020). Nested Neuronal Dynamics Orchestrate a Behavioral Hierarchy across Timescales. Neuron *105*, 562–576. https://doi.org/10.1016/j.neuron.2019.10.037.

37. White, J.G., Southgate, E., Thomson, J.N., and Brenner, S. (1986). The structure of the nervous system of the nematode Caenorhabditis elegans. Philos. Trans. R. Soc. Lond., B Biol. Sci. *314*, 1–340. https://doi.org/10.1098/rstb.1986.0056.

38. Cook, S.J., Jarrell, T.A., Brittin, C.A., Wang, Y., Bloniarz, A.E., Yakovlev, M.A., Nguyen, K.C.Q., Tang, L.T.H., Bayer, E.A., Duerr, J.S., et al. (2019). Whole-animal connectomes of both Caenorhabditis elegans sexes. Nature *571*, 63–71. https://doi.org/10.1038/s41586-019-1352-7.

39. Witvliet, D., Mulcahy, B., Mitchell, J.K., Meirovitch, Y., Berger, D.R., Wu, Y., Liu, Y., Koh, W.X., Parvathala, R., Holmyard, D., et al. (2021). Connectomes across development reveal principles of brain maturation. Nature *596*, 257–261. https://doi.org/10.1038/s41586-021-03778-8.

40. Shen, Y., Wen, Q., Liu, H., Zhong, C., Qin, Y., Harris, G., Kawano, T., Wu, M., Xu, T., Samuel, A.D., et al. (2016). An extrasynaptic GABAergic signal modulates a pattern of forward movement in Caenorhabditis elegans. eLife *5*, e14197. https://doi.org/10.7554/eLife.14197.

41. McIntire, S.L., Jorgensen, E., Kaplan, J., and Horvitz, H.R. (1993). The GABAergic nervous system of Caenorhabditis elegans. Nature *364*, 337–341. https://doi.org/10.1038/364337a0.

42. Huo, J., Xu, T., Liu, Q., Polat, M., Kumar, S., Zhang, X., Leifer, A.M., and Wen, Q. (2024). Hierarchical behavior control by a single class of interneurons. Proc. Natl. Acad. Sci. USA *121*, e2410789121. https://doi.org/10.1073/pnas.2410789121.

43. Wen, Q., Gao, S., and Zhen, M. (2018). Caenorhabditis elegans excitatory ventral cord motor neurons derive rhythm for body undulation. Philos. Trans. R. Soc. Lond., B Biol. Sci. *373*, 20170370. https://doi.org/10.1098/rstb.2017.0370.

44. Kawano, T., Po, M.D., Gao, S., Leung, G., Ryu, W.S., and Zhen, M. (2011). An imbalancing act: gap junctions reduce the backward motor circuit activity to bias C. elegans for forward locomotion. Neuron *72*, 572–586. https://doi.org/10.1016/j.neuron.2011.09.005.

45. Wen, Q., Po, M.D., Hulme, E., Chen, S., Liu, X., Kwok, S.W., Gershow, M., Leifer, A.M., Butler, V., Fang-Yen, C., et al. (2012). Proprioceptive Coupling within Motor Neurons Drives C. elegans Forward Locomotion. Neuron *76*, 750–761. https://doi.org/10.1016/j.neuron.2012.08.039.

46. Gao, S., Guan, S.A., Fouad, A.D., Meng, J., Kawano, T., Huang, Y.C., Li, Y., Alcaire, S., Hung, W., Lu, Y., et al. (2018). Excitatory motor neurons are local oscillators for backward locomotion. eLife *7*, e29915. https://doi.org/10.7554/eLife.29915.

47. Fouad, A.D., Teng, S., Mark, J.R., Liu, A., Alvarez-Illera, P., Ji, H., Du, A., Bhirgoo, P.D., Cornblath, E., Guan, S.A., et al. (2018). Distributed rhythm generators underlie Caenorhabditis elegans forward locomotion. eLife *7*, e29913. https://doi.org/10.7554/eLife.29913.

48. Marder, E., Bucher, D., Schulz, D.J., and Taylor, A.L. (2005). Invertebrate Central Pattern Generation Moves along. Curr. Biol. *15*, R685–R699. https://doi.org/10.1016/j.cub.2005.08.022.

49. Goulding, M. (2009). Circuits controlling vertebrate locomotion: moving in a new direction. Nat. Rev. Neurosci. *10*, 507–518. https://doi.org/10.1038/nrn2608.

50. Gray, J.M., Hill, J.J., and Bargmann, C.I. (2005). A circuit for navigation in Caenorhabditis elegans. Proc. Natl. Acad. Sci. USA *102*, 3184–3191. https://doi.org/10.1073/pnas.0409009101.

51. Kocabas, A., Shen, C.H., Guo, Z.V., and Ramanathan, S. (2012). Controlling interneuron activity in Caenorhabditis elegans to evoke chemotactic behaviour. Nature *490*, 273–277. https://doi.org/10.1038/nature11431.

52. Ouellette, M.H., Desrochers, M.J., Gheta, I., Ramos, R., and Hendricks, M. (2018). A gate-and-switch model for head orientation behaviors in Caenorhabditis elegans. eNeuro *5*. ENEURO.0121-18.2018. https://doi.org/10.1523/ENEURO.0121-18.2018.

53. Liu, H., Yang, W., Wu, T., Duan, F., Soucy, E., Jin, X., and Zhang, Y. (2018). Cholinergic Sensorimotor Integration Regulates Olfactory Steering. Neuron *97*, 390–405. https://doi.org/10.1016/j.neuron.2017.12.003.

54. Wang, Y., Zhang, X., Xin, Q., Hung, W., Florman, J., Huo, J., Xu, T., Xie, Y., Alkema, M.J., Zhen, M., et al. (2020). Flexible motor sequence generation during stereotyped escape responses. eLife *9*, e56942. https://doi.org/10.7554/eLife.56942.

55. Matsumoto, A., Toyoshima, Y., Zhang, C., Isozaki, A., Goda, K., and Iino, Y. (2024). Neuronal sensorimotor integration guiding salt concentration navigation in Caenorhabditis elegans. Proc. Natl. Acad. Sci. USA *121*, e2310735121. https://doi.org/10.1073/pnas.2310735121.

56. Kramer, T.S., Wan, F.K., Pugliese, S.M., Atanas, A.A., Pradhan, S., Hiser, A.W., Godinez, L.M., Luo, J., Bueno, E., Felt, T., and Flavell, S.W. (2026). Neural Sequences Underlying Directed Turning in *Caenorhabditis elegans*. Nat Neurosci. https://doi.org/10.1038/s41593-026-02257-5.

57. Dragomiretskiy, K., and Zosso, D. (2014). Variational Mode Decomposition. IEEE Trans. Signal Process. *62*, 531–544. https://doi.org/10.1109/TSP.2013.2288675.

58. Takens, F. (1981). Detecting Strange Attractors in Turbulence. In Dynamical Systems and Turbulence, D.A. Rand, and L.-S. Young, eds. (Springer), pp. 366–381.

59. Gray, J., and Hancock, G.J. (1955). The Propulsion of Sea-Urchin Spermatozoa. J. Exp. Biol. *32*, 802–814. https://doi.org/10.1242/jeb.32.4.802.

60. Fang-Yen, C., Wyart, M., Xie, J., Kawai, R., Kodger, T., Chen, S., Wen, Q., and Samuel, A.D.T. (2010). Biomechanical analysis of gait adaptation in the nematode Caenorhabditis elegans. Proc. Natl. Acad. Sci. USA *107*, 20323–20328. https://doi.org/10.1073/pnas.1003016107.

61. Johnson, R.E., and Brokaw, C.J. (1979). Flagellar hydrodynamics. A comparison between resistive-force theory and slender-body theory. Biophys. J. *25*, 113–127. https://doi.org/10.1016/S0006-3495(79)85281-9.

62. Boyle, J.H., Berri, S., and Cohen, N. (2012). Gait Modulation in C. elegans: An Integrated Neuromechanical Model. Front. Comput. Neurosci. *6*, 10. https://doi.org/10.3389/fncom.2012.00010.

63. Keaveny, E.E., and Brown, A.E.X. (2017). Predicting path from undulations for C. elegans using linear and nonlinear resistive force theory. Phys. Biol. *14*, 2. https://doi.org/10.1088/1478-3975/aa5ce6.

64. Costa, A.C., Ahamed, T., Jordan, D., and Stephens, G.J. (2024). A Markovian dynamics for Caenorhabditis elegans behavior across scales. Proc. Natl. Acad. Sci. USA *121*, e2318805121. https://doi.org/10.1073/pnas.2318805121.

65. Karbowski, J., Schindelman, G., Cronin, C.J., Seah, A., and Sternberg, P.W. (2008). Systems level circuit model of C. elegans undulatory locomotion: mathematical modeling and molecular genetics. J. Comput. Neurosci. *24*, 253–276. https://doi.org/10.1007/s10827-007-0054-6.

66. Shen, X.N., Sznitman, J., Krajacic, P., Lamitina, T., and Arratia, P.E. (2012). Undulatory Locomotion of Caenorhabditis elegans on Wet Surfaces. Biophys. J. *102*, 2772–2781. https://doi.org/10.1016/j.bpj.2012.05.012.

67. Rabets, Y., Backholm, M., Dalnoki-Veress, K., and Ryu, W.S. (2014). Direct Measurements of Drag Forces in C. elegans Crawling Locomotion. Biophys. J. *107*, 1980–1987. https://doi.org/10.1016/j.bpj.2014.09.006.

68. Ji, H., Fouad, A.D., Teng, S., Liu, A., Alvarez-Illera, P., Yao, B., Li, Z., and Fang-Yen, C. (2021). Phase response analyses support a relaxation oscillator model of locomotor rhythm generation in Caenorhabditis elegans. eLife *10*, e69905. https://doi.org/10.7554/eLife.69905.

69. Mellem, J.E., Brockie, P.J., Madsen, D.M., and Maricq, A.V. (2008). Action potentials contribute to neuronal signaling in C. elegans. Nat. Neurosci. *11*, 865–867. https://doi.org/10.1038/nn.2131.

70. Holló, G., and Novák, M. (2012). The manoeuvrability hypothesis to explain the maintenance of bilateral symmetry in animal evolution. Biol. Direct *7*, 22. https://doi.org/10.1186/1745-6150-7-22.

71. Akanyeti, O., Thornycroft, P.J., Lauder, G.V., Yanagitsuru, Y.R., Peterson, A.N., and Liao, J.C. (2016). Fish optimize sensing and respiration during undulatory swimming. Nat. Commun. *7*, 11044. https://doi.org/10.1038/ncomms11044.

72. Tingle, J.L., Garner, K.L., and Astley, H.C. (2024). Functional diversity of snake locomotor behaviors: A review of the biological literature for bioinspiration. Ann. N. Y. Acad. Sci. *1533*, 16–37. https://doi.org/10.1111/nyas.15109.

73. Wang, W., Comite, A.D., Voloshina, A., Daley, M., and Seethapathi, N. (2025). Deep Learning Framework for Action Prediction Reveals Multi-timescale Locomotor Control. Preprint at arXiv.

74. De Comite, A., and Seethapathi, N. (2025). Foot placement control underlies stable locomotion across species. Proc. Natl. Acad. Sci. USA *122*, e2413958122. https://doi.org/10.1073/pnas.2413958122.

75. Kam, K., Worrell, J.W., Janczewski, W.A., Cui, Y., and Feldman, J.L. (2013). Distinct Inspiratory Rhythm and Pattern Generating Mechanisms in the preBötzinger Complex. J. Neurosci. *33*, 9235–9245. https://doi.org/10.1523/JNEUROSCI.4143-12.2013.

76. Phillips, R.S., and Rubin, J.E. (2022). Putting the theory into 'burstlet theory' with a biophysical model of burstlets and bursts in the respiratory preBötzinger complex. eLife *11*, e75713. https://doi.org/10.7554/eLife.75713.

77. Kim, D., Park, S., Mahadevan, L., and Shin, J.H. (2011). The shallow turn of a worm. J. Exp. Biol. *214*, 1554–1559. https://doi.org/10.1242/jeb.052092.

78. Soh, Z., Sakamoto, K., Suzuki, M., Iino, Y., and Tsuji, T. (2018). A computational model of internal representations of chemical gradients in environments for chemotaxis of Caenorhabditis elegans. Sci. Rep. *8*, 17190. https://doi.org/10.1038/s41598-018-35157-1.

79. Lockery, S.R. (2011). The computational worm: spatial orientation and its neuronal basis in C. elegans. Curr. Opin. Neurobiol. *21*, 782–790. https://doi.org/10.1016/j.conb.2011.06.009.

80. Atanas, A.A., Kim, J., Wang, Z., Bueno, E., Becker, M., Kang, D., Park, J., Kramer, T.S., Wan, F.K., Baskoylu, S., et al. (2023). Brain-wide representations of behavior spanning multiple timescales and states in C. elegans. Cell *186*, 4134–4151. https://doi.org/10.1016/j.cell.2023.07.035.

81. Brenner, S. (1974). The genetics of Caenorhabditis elegans. Genetics *77*, 71–94. https://doi.org/10.1093/genetics/77.1.71.

82. Qi, Y.B., Garren, E.J., Shu, X., Tsien, R.Y., and Jin, Y. (2012). Photo-inducible cell ablation in Caenorhabditis elegans using the genetically encoded singlet oxygen generating protein miniSOG. Proc. Natl. Acad. Sci. USA *109*, 7499–7504. https://doi.org/10.1073/pnas.1204096109.

83. Xu, S., and Chisholm, A.D. (2016). Highly efficient optogenetic cell ablation in C. elegans using membrane-targeted miniSOG. Sci. Rep. *6*, 21271. https://doi.org/10.1038/srep21271.

84. Leifer, A.M., Fang-Yen, C., Gershow, M., Alkema, M.J., and Samuel, A.D.T. (2011). Optogenetic manipulation of neural activity in freely moving Caenorhabditis elegans. Nat. Methods *8*, 147–152. https://doi.org/10.1038/nmeth.1554.

85. Li, J., Shang, Z., Chen, J.H., Gu, W., Yao, L., Yang, X., Sun, X., Wang, L., Wang, T., Liu, S., et al. (2023). Engineering of NEMO as calcium indicators with large dynamics and high sensitivity. Nat. Methods *20*, 918–924. https://doi.org/10.1038/s41592-023-01852-9.

86. Fraser, A.M., and Swinney, H.L. (1986). Independent coordinates for strange attractors from mutual information. Phys. Rev. A Gen. Phys. *33*, 1134–1140. https://doi.org/10.1103/PhysRevA.33.1134.

87. Rhodes, C., and Morari, M. (1997). False-nearest-neighbors algorithm and noise-corrupted time series. Phys. Rev., E *55*, 6162–6170. https://doi.org/10.1103/PhysRevE.55.6162.

Please cite this article in press as: Li et al., Multi-timescale motor circuit dynamics underlie adaptive and efficient exploratory behavior, Current Biology (2026), https://doi.org/10.1016/j.cub.2026.05.004

STAR★METHODS

KEY RESOURCES TABLE

REAGENT or RESOURCE	SOURCE	IDENTIFIER
Bacterial and virus strains		
Escherichia coli: Strain OP50	Caenorhabditis Genetics Center	OP50
Experimental models: Organisms/strains		
C. elegans: Wild-type Bristol N2	Caenorhabditis Genetics Center	N2
C. elegans: *wenEx1101[Prig-5a::PH-miniSOG::wCherry, Plin-44::mCherry]*	This study	WEN1101
C. elegans: *wenEx1037[Pflp-22δ4::PH-miniSOG::wCherry];*	This study	WEN1037
C. elegans: *wenEx1119[Podr-2(18)::TOMM20-miniSOG::wCherry, Plin-44::mCherry]*	This study	WEN1119
C. elegans: *wenEx1124[Prig-5a::PH-miniSOG::wCherry, Podr-2(18)::TOMM20-miniSOG::wCherry, Plin-44::mCherry]*	This study	WEN1124
C. elegans: *wenEx1111[Prig-5a::PH-miniSOG::wCherry, Pflp-22δ4::PH-miniSOG::wCherry, Punc-122::RFP]*	This study	WEN1111
C. elegans: *wenEx1123[Pflp-22δ4::PH-miniSOG::wCherry, Podr-2(18)::TOMM20-miniSOG::wCherry, Plin-44::GFP]*	This study	WEN1123
C. elegans: *wenEx1112[Pflp-22δ4::GtACR2::GFP, Plin-44::mCherry]*	This study	WEN1112
C. elegans: *wenEx1120[Podr-2(18)::TOMM20-miniSOG::wCherry, Prig-5a::PH-miniSOG::wCherry, Pflp-22δ4::PH-miniSOG::wCherry, Plin-44::mCherry]*	This study	WEN1120
C. elegans: *yxIs30[Punc-47::Arch::eGFP]*	Shen et al.[40]	ZC2430
C. elegans: *wenEx0951[Plad-2::Cre, Plim-4(-3328–2174)v1p1::LoxP::PBSTOP::LoxP::TOMM20-miniSOG::wCherry, Plin-44::mCherry]*	Huo et al.[42]	WEN0951
C. elegans: *wenEx1138[Prig-5a::wNEMOs, Prig-5a::wCherry, Plin-44::GFP]*	This study	WEN1138
C. elegans: *wenEx1036[Pmyo-3::Arch::wCherry]*	This study	WEN1036
C. elegans: *wenEx1035[Punc-4::twk-18::wCherry]*	This study	WEN1035
C. elegans: *unc-7(e5)X; unc-9(fc16); wenEx1126[Punc-4::twk-18::wCherry, Plin44::mCherry]*	This study	WEN1126
Recombinant DNA		
Prig-5a::PH-miniSOG::wCherry	This study	quan0180
Pflp-22δ4::PH-miniSOG::wCherry	This study	quan0771
Podr-2(18)::TOMM20-miniSOG::wCherry	This study	quan0200
Pflp-22δ4::GtACR2::GFP	This study	quan0772
Plim-4(-3328–2174)v1p1::LoxP::PBSTOP::LoxP::TOMM20-miniSOG::wCherry	Huo et al.[42]	quan0729
Plad-2::Cre	Huo et al.[42]	quan0421
Prig-5a::wNEMOs	This study	quan1021
Prig-5a::wCherry	This study	quan1022
Pmyo-3::Arch::wCherry	This study	quan0124
Punc-4::twk-18::wCherry	Kawano et al.[44]	pJH2108

(*Continued on next page*)

Please cite this article in press as: Li et al., Multi-timescale motor circuit dynamics underlie adaptive and efficient exploratory behavior, Current Biology (2026), https://doi.org/10.1016/j.cub.2026.05.004

Continued		
REAGENT or RESOURCE	SOURCE	IDENTIFIER
Punc-122::RFP	Huo et al.[42]	quan0232
Plin-44::GFP	Huo et al.[42]	quan0051
Plin-44::mCherry	Huo et al.[42]	quan0134
Software and algorithms		
MATLAB	MathWorks	RRID: SCR_001622
Python3.8	Python	RRID: SCR_008394
ImageJ	NIH Image	RRID: SCR_003070
Code for the head circuit model	This study	10.5281/zenodo.19794971

EXPERIMENTAL MODEL AND STUDY PARTICIPANT DETAILS

C. elegans strains were grown and maintained on nematode growth media (NGM) plates seeded with the *Escherichia coli* strain OP50 at 16-22 °C.

METHOD DETAILS

C. elegans strains

C. elegans strains were cultivated by standard procedures.[81] Transgenic animals in optogenetic experiments were cultivated in the dark on NGM plates with OP50 bacteria and all-trans-retinal (ATR) for over 8 hrs. We used young adult hermaphrodites to carry out all the experiments.

Molecular biology

We used standard molecular biology methods. Promoters P*rig-5a* (2.2 kb), Pflp-*22p*-Δ*4* (1.5 kb), and P*odr-2* were amplified by PCR from the N2 genome.

Behaviour recording

We recorded *C. elegans* behaviours on 0.8% (wt/vol) M9 agar plate. Before recording, the animals were first transferred to a sterile NGM plate to eliminate the OP50 bacteria, then transferred to another sterile NGM plate for 25-35 min to make more frequent forward movements. The animals also acclimatized to the M9 agar for 2-3 min. Then we recorded freely moving animals for 5-15 min. Under dark field infrared illumination, the animals were automatically tracked and retained within the field of view of a 10X objective on a Nikon inverted microscope (Ti-U, Japan). Behaviors were recorded by a Basler CMOS camera (aca2000-340kmNIR, Germany). We used MATLAB custom software (MathWorks, Inc Natick, MA, USA) to process the behavioral data afterwards.

Optogenetic ablation

We used a mitochondrial-targeted miniSOG (TOMM20-miniSOG)[82] or a membrane-targeted miniSOG (PH-miniSOG)[83] to ablate specific neurons in *C. elegans*. Late L4/early young adult transgenic animals were transferred to an unseeded NGM plate, on which the animals were restricted by a 1 cm diameter filter paper ring soaked with 100 μM $CuCl_2$. The animals were then illuminated for 5 min using pulse blue LED (M470L3-C5; Thorlabs) light (0.5 s on and 0.5 s off) at an intensity of 2.0 mW/mm^2. After illumination, animals were transplanted to an OP50-seeded NGM plate and recovered for 4 hours before behaviour recording. Confocal imaging at 60x magnification was performed immediately after behavior recording. Ablated neurons showed irregular morphology and scattered fluorescent debris, unlike the intact elliptical or circular shapes of non-ablated neurons.

Optogenetics

Lasers and a digital micromirror device (DLI4130 0.7 XGA, Digital Light Innovations, TX, USA) were used to generate spatiotemporal optogenetic manipulations[84] at a specific wavelength (473 nm, 561 nm or 635 nm). We manipulated the activities of neurons through light-activated channels (GtACR2, Arch, or Chrimson). Each animal was stimulated 5–8 times with at least a 40-second inter-stimulus interval.

Behavioural analysis

We exclusively analyzed the forward movement. Forward-moving frames were manually labeled and further processed in MATLAB to quantify parameters. Forward movement was identified when the trajectory of an animal remained straight or turned no more than 90 degrees.

Please cite this article in press as: Li et al., Multi-timescale motor circuit dynamics underlie adaptive and efficient exploratory behavior, Current Biology (2026), https://doi.org/10.1016/j.cub.2026.05.004

The animal orientation is the average angle between the x-axis of the camera frame and the 100 centerline segments. To quantify orientation changes during forward movement, the following steps were executed:

1. The curvature vectors of the centerlines were projected onto the first two principal components, producing two-dimensional postural representations denoted as $a_1(t)$ and $a_2(t)$. 2. The phase of forward movement (Φ) was computed with $\Phi = \text{angle}(a_1 + i \cdot a_2)$, with zero-phase instances occurring when a_1 is at its maximum and a_2 is zero. 3. Orientation changes were measured between zero-phase moments separated by three cycles.

Calcium imaging

Calcium imaging was performed in animals that expressed wNEMOs[85] and wCherry proteins in the same neurons. The measurement of calcium activity was achieved by calculating a ratiometric change, which is defined as the fluorescence ratio of the green channel and the reference channel $\Delta R(t)/R_0$ (wNEMOs / wCherry), where R_0 is the baseline ratio. We found NEMOs superior to GCaMP for capturing RMD calcium activity. Due to the broader emission spectrum of wNEMOs, which caused fluorescence bleed-through into the reference channel (wCherry), we corrected the activity ratio using the following equation

$$R = \frac{F_g}{F_r - \epsilon_g \times F_g},$$

where F_g represents the fluorescence intensity of the green channel, F_r represents the fluorescence intensity of the reference channel, ϵ_g is the bleed-through coefficient of wNEMOs, which could be 0.08 to 0.20 under different experimental conditions.

To effectively capture calcium activity in RMD neurons during behavioral state transitions in freely moving animals crawling on a 2% (wt/vol) NGM agarose plate with a coverslip, calcium imaging was performed using a wide-field fluorescence microscope with a 20X objective (Nikon S Plan Fluor, WD = 7.4mm, NA = 0.45, Japan), which had a large imaging field (0.65 mm × 0.65 mm). To minimize motion artifacts and improve calcium activity recording in RMDL/R neurons during head swings, we immobilized the body in a microfluidic channel allowing only the head to move (Figure S5), and employed a 60X water immersion objective (Nikon Plan Apo, WD = 0.27mm, NA = 1.2, Japan) for enhanced resolution instead of a 20X objective. This objective was mounted on a piezoelectric scanner (Physik Instrumente, Germany) for z-axis neuron scanning. Blue light (488 nm) and green light (561 nm) were introduced to excite wNEMOs and wCherry proteins, respectively. Green and red emission signals were captured by the objective, separated by a dichroic mirror, and projected onto sCMOS sensors (Andor Zyla 4.2, UK). The two-channel images were processed by custom-written MATLAB scripts.

Circuit Model

The head circuit model consists of two parallel neuronal groups that innervate the head muscle: the RMD group and the SMD-SMB group. These groups utilize proprioceptive feedback from different timescales to modulate their states and output. The RMD group integrates rapid feedback from upstream mechanosensitive neurons, which are likely to detect head movements. Specifically, this fast feedback signal K^{fast} is a low-pass filtered version of head curvature κ.

$$\tau_f \frac{dK^{\text{fast}}}{dt} = -K^{\text{fast}} + \kappa.$$

On the other hand, the SMD-SMB group receives slow feedback K^{slow} from posterior curvature, presumably detected by their posterior sublateral processes. This slow feedback signal K^{slow} is a low-pass filtered version of the surrogate posterior curvature κ', which is a slow integration of head curvature:

$$\begin{aligned} \tau_s \frac{d\kappa'}{dt} &= -\kappa' + a^s \kappa \\ \tau_f \frac{dK^{\text{slow}}}{dt} &= -K^{\text{slow}} + \kappa' \end{aligned},$$

where the fast and slow time constants, $\tau_f = 0.3s$ and $\tau_s = 0.8s$, reflect the fast nature of neuronal activity and the relative slowness of head-to-neck bending propagation. The parameter a^s determines the amplitude of surrogate posterior curvature κ'.

The bistable dynamics of the SMD-SMB group are represented using a hysteresis curve (Figure 7A middle):

$$U_t^{\text{SMD\&SMB}}\left(K^{\text{slow}}\right) = \begin{cases} -1 & K^{\text{slow}} > \theta_s \\ 1 & K^{\text{slow}} < -\theta_s \\ U_{t-1}^{\text{SMD\&SMB}} & \text{else} \end{cases}.$$

When the slow feedback K^{slow} exceeds θ_s (sustained dorsal bending), the neuronal output $U_t^{\text{SMD\&SMB}}(x)$ switches to ventral muscle activation (lower branch in Figure 7A, middle), while feedbacks below $-\theta_s$ trigger dorsal muscle activation (upper branch).

The voltage supplied to RMD neurons (RMD-D/L/R for dorsal muscles and RMD-V/L/R for ventral muscles) follows a Heaviside step function based on fast feedback. The overlapping L/R designation indicates that left (L) and right (R) RMD neurons contribute

Please cite this article in press as: Li et al., Multi-timescale motor circuit dynamics underlie adaptive and efficient exploratory behavior, Current Biology (2026), https://doi.org/10.1016/j.cub.2026.05.004

to both dorsal and ventral head muscle innervation, though their precise functional roles remain incompletely characterized. The relative synaptic strengths and specific contribution patterns of L and R RMD neurons to directional head movements require further investigation to fully elucidate their functional specialization.

$$U^{\mathrm{RMDD/L/R}}\left(K^{\mathrm{fast}}\right) = \begin{cases} 1 & K^{\mathrm{fast}} < -\theta_f \\ 0 & K^{\mathrm{fast}} > -\theta_f \end{cases} U^{\mathrm{RMDV/L/R}}\left(K^{\mathrm{fast}}\right) = \begin{cases} 1 & K^{\mathrm{fast}} > \theta_f \\ 0 & K^{\mathrm{fast}} < \theta_f \end{cases}.$$

The combined neuronal outputs activate the muscle and drive the head bending:

$$\tau_M \frac{dM}{dt} = -M + U_t^{\mathrm{SMD\&SMB}}\left(K^{\mathrm{slow}}\right) + cU^{\mathrm{RMDD/L/R}}\left(K^{\mathrm{fast}}\right) - cU^{\mathrm{RMDV/L/R}}\left(K^{\mathrm{fast}}\right)$$
$$\tau_\kappa \frac{d\kappa}{dt} = -\kappa + M \qquad \text{(Equation 2)}$$

Positive M and κ represent dorsal muscle activation and dorsal bending, respectively. The RMDD/L/R neurons sense ventral bending ($K^{\mathrm{fast}} < 0$) and drive dorsal bending, contributing $U^{\mathrm{RMDD/L/R}}\left(K^{\mathrm{fast}}\right)$. Conversely, RMDV/L/R neurons contribute $-U^{\mathrm{RMDV/L/R}}\left(K^{\mathrm{fast}}\right)$. The coefficient c scales the contribution of the RMD group.

We determined the head's mechanical time constant τ_κ through relaxation experiments. Following optogenetic activation of unilateral head muscles, we analyzed the decrease in head curvature after the termination of head muscle activation. By fitting exponential functions to these relaxation curves, we found that the head returns to its resting position with a characteristic timescale of 0.4 seconds. This rapid relaxation is notably faster than the body's mechanical time constant,[60] likely due to the head's lower mechanical load. The head's quick response dynamics proved essential for generating the rapid head casts captured in our model. The time constant for muscle activation τ_M is 0.1 seconds following previous works.[62,68]

We examined how well our model's surrogate posterior curvature aligned with the actual posterior curvature of animals. To do this, we compared two time lags: (1) the lag between head and neck curvature in N2 animals, and (2) the lag between head and surrogate posterior curvature in our model. We determined these lags by identifying the time point at which the cross-correlation between the head curvature's slow mode and the posterior curvature signal reached its maximum.

Simulated RMD ablation was implemented by removing the contributions from $U^{\mathrm{RMDD/L/R}}$ and $U^{\mathrm{RMDV/L/R}}$ by setting $c = 0$. The simulated neck inhibition was implemented by scaling the slow feedback K^{slow} by setting $a_s \leftarrow 0.6a_s$.

Neuro-mechanical Model

To investigate the impact of the temporal pattern of head bending on the curvature amplitude of the rest of the body, we employed a bio-realistic mechanical model from[62] to simulate forward locomotion. We proposed a ventral nerve cord (VNC) circuit featuring bistable motor neuron pairs and anterior proprioceptive coupling to drive this mechanical model.

The mechanical model[62] comprises 48 connected mechanical units, with the body wall muscles modeled as elastic rods capable of active contraction. The model is controlled by 12 pairs of dorsal and ventral B-type motor neurons, with each pair governing 4 mechanical units.

The dynamics of each pair of B-type body motor neurons is governed by two main mechanisms:

Dorsal contraction in the anterior units activates the dorsal motor neuron, and ventral contraction activates the ventral motor neuron.
Reciprocal inhibition exists between the dorsal and ventral motor neuron partners.

We used directional proprioceptive coupling[45] to induce an activation of motor neurons through anterior bending curvature changes (Figure S12A). The mutually inhibiting neuron pairs operate within a bistable regime, modulated by the curvature in the anterior section of the body (Figure S12B).

Let $S_t = 1$ represent the dorsal domination, and $S_t = -1$ represent the ventral domination. The proprioceptive signal P, which is equal to the mean curvature of anterior 8 units (48 units in total), switches the motor neuron pair between dorsal domination and ventral domination:

$$S_t = \begin{cases} -S_{t-1} & \text{if } P > P_{th} \text{ or } P < -P_{th} \\ S_{t-1} & \text{else} \end{cases}.$$

Here, P is positive for anterior dorsal bending and negative for ventral bending. When $S = 1$, the dorsal motor neuron dominates (Figure S12B upper and lower branches for U_D and U_V, respectively):

$$\begin{aligned} U_D &= g(P - P_{th}) + U_b \\ U_V &= 0 \end{aligned}.$$

Conversely, when $S = -1$, the ventral motor neuron is activated (Figure S12B, lower and upper branches for U_D and U_V, respectively):

$$\begin{aligned} U_D &= 0 \\ U_V &= -g(P + P_{th}) + U_b \end{aligned}.$$

Please cite this article in press as: Li et al., Multi-timescale motor circuit dynamics underlie adaptive and efficient exploratory behavior, Current Biology (2026), https://doi.org/10.1016/j.cub.2026.05.004

Here, U_D and U_V denote the activation levels of the dorsal and ventral motor neurons, respectively. U_b is the baseline activation, and g modulates how the activation level changes with proprioception. We set $g > 0$ so that deeper anterior bending leads to higher motor neuron activity and thus deeper posterior bending. This activation function helps to propagate the change in the head bending amplitude along the body.

Finally, the activation of the foremost motor neuron pair, which drives head bending, is controlled by an external input u_t, which alternates between 1 and -1 i.e., between dorsal activation and ventral activation:

$$U_D^0, U_V^0 = \begin{cases} U_{\text{head}}, 0 & u_t = 1 \\ 0, U_{\text{head}} & u_t = -1 \end{cases}.$$

The head input is simplified to a binary signal to capture rapid head casts, which are more likely due to abrupt changes in head motor neuron output rather than gradual gain modulation.[51,52]

Using our neuro-mechanical model, we can simulate forward locomotion by applying periodic input to the head motor neurons. Our goal is to identify the input pattern that maximizes kinematic efficiency, defined as the ratio of the average locomotion speed to the undulation frequency. This efficiency measure represents the distance the animal covers in one undulation period.

To explore possible input patterns, we discretized one period of the head input signal into 20 intervals, resulting in a binary sequence of length 20. To further constrain the search space, we imposed dorsal-ventral symmetry around the midpoint and limited the number of transitions between dorsal and ventral activation to no more than two in half a period. These constraints reduced the number of possible input signal profiles to 72. Among these profiles, we identified the one that yielded the highest kinematic efficiency.

Phase space reconstruction

To analyze the dynamics of head movement, we employed phase space reconstruction using time-delay embedding, a technique based on Takens' theorem.[58] This method allows us to reconstruct the multidimensional phase space from our one-dimensional time series of head curvature $\kappa(t)$.

To estimate the optimal time delay τ and embedding dimension m, we used MATLAB *phaseSpaceReconstruction* toolbox, which uses Average Mutual Information (AMI)[86] and False Nearest Neighbor (FNN) algorithm[87] to determine the delay time τ and embedding dimension m, respectively.

With τ and m determined, we constructed the phase space vector $y(t)$ from the time series $\kappa(t)$ as follows:

$$y(t) = [\kappa(t), \kappa(t+\tau), \kappa(t+2\tau), ..., \kappa(t+(m-1)\tau)].$$

This process transforms our one-dimensional time series into a set of m-dimensional vectors.

To visualize the topological feature of the reconstructed phase space, we projected the m-dimensional vectors into the space spanned by three principal components. For better visualization, we then fitted the density plots using kernel density estimation with a Gaussian kernel, whose optimal bandwidth was determined by the MATLAB *ksdensity* function.

This reconstructed phase space provides a geometric representation of the system's dynamics, allowing us to identify features such as attractors, periodic orbits, or chaos, which are not apparent in the original time series.

Optimal angle of attack for maximum locomotion speed

We describe the traveling body wave along the moving direction with $y = b \sin\frac{2\pi}{\lambda_x}(x - V_W t) = b \sin\frac{2\pi}{\lambda_x}(x - f\lambda_x t)$, where b is the body wave amplitude, λ_x is the effective wavelength along the moving direction, $V_W = f\lambda_x$ is the wave speed, and f is the undulation frequency. For simplicity, the number of complete waves is one in this derivation.

It is crucial to distinguish between the effective wavelength and the wavelength in the body length coordinate used in previous works.[59,60] While these wavelengths are similar for small amplitudes, they diverge as the amplitude increases. This divergence occurs because the effective wavelength decreases due to the shrinkage along the anterior-posterior axis in a more curled posture. The sine wave amplitude b and effective wavelength λ_x are related by a constant body length:

$$L = \int_0^{\lambda_x} \left(1+\left(\frac{dy}{dx}\right)^2\right)^{\frac{1}{2}} dx = \lambda_x \int_0^1 \left(1+\left(\frac{2\pi b}{\lambda_x}\right)^2 \cos^2(2\pi x')\right)^{\frac{1}{2}} dx'.$$

Follow Gray and Hancock,[59] the resistive force on an element ds along the moving axis is given by:

$$dF = \left\{ \frac{(C_N - C_L)\frac{dy}{dt}\frac{dy}{dx} - V_x\left[C_L + C_N\left(\frac{dy}{dx}\right)^2\right]}{1+\left(\frac{dy}{dx}\right)^2} \right\} ds.$$

For large amplitude, we have $ds = \sqrt{1+(dy/dx)^2}dx$ thus:

$$dF = \left\{ \frac{(C_N - C_L)\frac{dy}{dt}\frac{dy}{dx} - V_x\left[C_L + C_N\left(\frac{dy}{dx}\right)^2\right]}{\left(1+\left(\frac{dy}{dx}\right)^2\right)^{\frac{1}{2}}} \right\} dx.$$

Total force over a complete wave is:

$$F = \int_0^{\lambda_x} dF.$$

We introduce integrals:

$$I = I(b,\lambda_x) = \int_0^{\lambda_x} \frac{1}{\left(1+\left(\frac{dy}{dx}\right)^2\right)^{\frac{1}{2}}} dx = \int_0^1 \frac{1}{\left(1+\left(\frac{2\pi b}{\lambda_x}\right)^2 \cos^2(2\pi x')\right)^{\frac{1}{2}}} dx',$$

$$J = J(b,\lambda_x) = \int_0^{\lambda_x} \frac{\left(\frac{dy}{dx}\right)^2}{\left(1+\left(\frac{dy}{dx}\right)^2\right)^{\frac{1}{2}}} dx = \int_0^1 \frac{\left(\frac{2\pi b}{\lambda_x}\right)^2 \cos^2(2\pi x')}{\left(1+\left(\frac{2\pi b}{\lambda_x}\right)^2 \cos^2(2\pi x')\right)^{\frac{1}{2}}} dx'.$$

Using the zero net force condition:

$$F = \int_0^{\lambda_x} dF = J(C_N - C_L)V_W - V_x(C_L I + C_N J) = 0.$$

The locomotion speed is derived as:

$$\frac{V_x}{V_W} = \frac{\frac{C_N}{C_L} - 1}{\frac{C_N}{C_L} + \frac{I}{J}}. \quad \text{(Equation 3)}$$

We then can numerically calculate the moving speed of the animal at an arbitrarily varying amplitude b, with a fixed frequency and with the wavenumber equal to 1:

$$V_x = \frac{\frac{C_N}{C_L} - 1}{\frac{C_N}{C_L} + \frac{I(b)}{J(b)}} f\lambda_x(b).$$

To further simplify the equation, we apply a small amplitude approximation to the integrals:

$$\frac{I(b)}{J(b)} \approx \frac{\lambda_x^2}{2\pi^2 b^2}.$$

The body angle α along the moving direction follows $\tan(\alpha) = \frac{dy}{dx} = \frac{2\pi b}{\lambda_x}\sin\frac{2\pi}{\lambda_x}(x - V_W t)$. The angle of attack A_a is defined as the maximum angle that follows

$$\tan A_a = \frac{2\pi b}{\lambda_x}.$$

Combining these, we arrive at:

$$V_x \approx \frac{\frac{C_N}{C_L} - 1}{\frac{C_N}{C_L} + \frac{\lambda_x^2}{2\pi^2 b^2}} f\lambda_x(b) = \frac{\frac{C_N}{C_L} - 1}{\frac{C_N}{C_L} + \frac{2}{\tan^2(A_a)}} f\lambda_x(b). \quad \text{(Equation 4)}$$

Our numerical analysis suggested that Equation 4, which incorporates the small amplitude approximation in the integrals and wavelength compensation (accounting for finite amplitude), closely approximates Equation 3.

We defined the kinematic efficiency as:

$$V_x \Big/ f = \frac{\frac{C_N}{C_L} - 1}{\frac{C_N}{C_L} + \frac{2}{\tan^2(A_a)}} \lambda_x(b). \quad \text{(Equation 5)}$$

That equals the distance covered by the animal in one period of undulation.

QUANTIFICATION AND STATISTICAL ANALYSIS

Kinematic analysis of head movements

We used custom-written MATLAB scripts to extract the timestamp, stage position, and centerline of an animal. The centerline of the animal was first divided into $N = 100$ segments and the orientation of each segment, $\theta(s), s = 1,2,\cdots,N$, was calculated. The curvature $K(s) = \Delta\theta(s)/\Delta s$ was calculated and then normalized into a dimensionless unit $K{\cdot}L$, where L is the body length. And the dimensionless head curvature κ was calculated as

$$\kappa = \frac{1}{50} \sum_{j=0}^{4} \sum_{i=1}^{10} K(i+j){\cdot}L. \quad \text{(Equation 6)}$$

We divided the animal into 100 segments rather than the 25 segments used in previous work,[36] leveraging our higher spatial resolution along the body axis. We defined the head region as the anterior 15% of the body (segments 1-15) and included all these segments in our curvature calculation, whereas previous studies excluded the most anterior segment due to noise concerns and began measurements from the second segment. Our approach of averaging across multiple anterior segments helps mitigate noise while preserving information from the animal's most anterior region, which is critical for capturing the full extent of head-bending dynamics.

The head bending amplitude of each forward run episode was calculated using the following procedure: 1. A reference amplitude was introduced as $A_{\text{ref}} = (\max(\kappa(t)) - \min(\kappa(t))/2$. 2. Using the scipy.signal package, we detected peaks in the curvature time series that exceeded the reference amplitude A_{ref} in prominence. These peaks correspond to maximum head-bending positions. The final amplitude was computed as the median of the absolute values of these identified peaks. The neck curvature is defined as the average curvature of the anterior 15%-30% region of the body and is calculated in the same way as the head curvature.

Variational mode decomposition

We use the variational mode decomposition, abbreviated as VMD,[57] to distinguish the fast and slow components of head bending dynamics. The head curvature signal was decomposed into five different intrinsic mode functions ($\kappa_i, i = 1,2,3,4,5$) with increasing central frequencies. The last mode κ_5, which has the highest frequency and negligible power, was excluded from further analysis. The remaining four modes can reconstruct the fast and slow dynamics of head bending: a fast dynamic mode $\kappa_f(t)$ is reconstructed by a linear combination of the modes 2–4, and a slow dynamic mode $\kappa_s(t)$ is identified by mode 1.

The power of each mode P_i was calculated as $P_i = \int_0^\infty p_i df, i = 1,2,3,4,5$, where p_i is the power spectrum density of mode i. Then, the power of the fast dynamic mode was calculated as $P_f = P_2 + P_3 + P_4$, while the power of the slow dynamic mode was calculated as $P_s = P_1$. Subsequently, the power ratio was calculated as $\frac{P_f}{P_f+P_s}$ for the fast dynamic mode and $\frac{P_s}{P_f+P_s}$ for the slow dynamic mode.

Head-cast analysis

The rapid oscillation superimposed on the slow dynamic mode can sometimes propagate backward along the anterior body, a phenomenon known as the head cast[36]. We extend this term to include smaller and rapid wiggles restricted to the very front part of the head.

Head-casts notably move opposite to the slow dynamic mode, identified in this study via a two-step process:

We identified zero-crossing points in the time derivative of a denoised head curvature time series $\dot{\kappa}(t)$, where $\kappa(t) = \kappa^s(t) + \kappa^f(t)$. We distinguished these time points: zero crossings after which the time derivatives of the denoised signal and the slow dynamic mode have opposite signs ($\text{sign}(\dot{\kappa}) = -\text{sign}\left(\dot{\kappa^s}\right)$) mark the start of a head cast

(Figure 2A). The next zero-crossing point is designated as the end of a head cast, after which $\text{sign}(\dot{\kappa}) = \text{sign}\left(\dot{\kappa^s}\right)$.

The head-cast amplitude was measured as the absolute difference in head curvature between the start and end points. The relative amplitude, the ratio of absolute amplitude to head bending magnitude of the forward run, was used to identify significant head casts with relative amplitudes greater than 0.3, thus filtering out the head casts originating from the noise of curvature measurement. The head casts frequency was calculated as the number of significant head casts per episode divided by the episode's duration in seconds.

To quantify the relationship between head casts and body undulation dynamics, we computed the joint distribution of head casts as a function of stroking amplitude and phase. We defined the phase of head bending using the slow dynamic mode, given its sinusoidal nature. Specifically, we used the instantaneous phase from its Hilbert transform. As we did not distinguish between dorsal and

Please cite this article in press as: Li et al., Multi-timescale motor circuit dynamics underlie adaptive and efficient exploratory behavior, Current Biology (2026), https://doi.org/10.1016/j.cub.2026.05.004

ventral bending directions, we denoted phase 0 as the point of maximum curvature and phase π as the point of minimum curvature in the slow mode. We discretized the amplitude and phase dimensions into uniform bins. For each bin, we counted the total number of head casts occurring when the animal's posture fell within that amplitude-phase range. The head cast density of each bin is calculated as the total number of head casts divided by the total duration of all trials.

Linear regression to relate head cast and turning angle

We use a linear model to capture the relationship between the head casts and the gradual turning angle that the animals perform. Head casts were grouped into six amplitude categories: <-6, -6 to -3, -3 to 0, 0 to 3, 3 to 6, and >6, with negative levels representing head casts in negative curvature and positive levels in positive curvature. For every three consecutive cycles, we recorded the orientation change and number of head casts from six amplitude categories. The head casts were linearly aggregated to create an impact vector. If a single head cast with an amplitude <-6 and two head casts with amplitudes between 3–6 occur during a period, the resulting head-cast impact vector would be [1, 0, 0, 0, 2, 0]. To quantify the contribution of head casts from six amplitude categories, we run a linear regression to obtain the linear coefficients using least squares. To estimate the uncertainty in the coefficients, we performed bootstrap resampling, generating 10,000 randomized datasets and corresponding coefficient sets. This approach provides a robust estimation of the model's parameter variability and statistical confidence.

To assess the contribution of slow mode amplitude to turning, we recorded the positive amplitude and negative amplitude of the slow mode during every three consecutive cycles. The positive and negative amplitude was calculated as the average of the top 5% and the bottom 5% of curvature values in that period. We ran linear regressions of orientation changes against (1) head cast amplitude alone, (2) slow mode amplitude alone, and (3) both factors combined.

Statistical test

Statistical tests were indicated in the figure legends, including methods, error bars, numbers of trials and animals, and p-values. Using MATLAB, we applied the Mann-Whitney U test and Student's T-test to determine the significance of the difference between the groups, and all multiple comparisons were adjusted using the Bonferroni correction.